Monthly Notices
of the
ROYAL ASTRONOMICAL SOCIETY

MNRAS **500,** 3213–3239 (2021)
Advance Access publication 2020 November 7

doi:10.1093/mnras/staa3329

2D kinematics of massive stars near the Galactic Centre

Mattia Libralato [1]★ Daniel J. Lennon,[2,3] Andrea Bellini,[1] Roeland van der Marel,[1,4] Simon J. Clark,[5] Francisco Najarro,[6] Lee R. Patrick [7] Jay Anderson,[1] Luigi R. Bedin [8] Paul A. Crowther,[9] Selma E. de Mink,[10,11] Christopher J. Evans,[12] Imants Platais,[13] Elena Sabbi[1] and Sangmo Tony Sohn[1]

[1]*Space Telescope Science Institute, 3700 San Martin Drive, Baltimore, MD 21218, USA*
[2]*Instituto de Astrofísica de Canarias, E-38205 La Laguna, Tenerife, Spain*
[3]*Departamento Astrofísica, Universidad de La Laguna, E-38206 La Laguna, Tenerife, Spain*
[4]*Center for Astrophysical Sciences, Department of Physics and Astronomy, Johns Hopkins University, Baltimore, MD 21218, USA*
[5]*School of Physical Sciences, The Open University, Walton Hall, Milton Keynes MK7 6AA, UK*
[6]*Centro de Astrobiología (CSIC/INTA), Ctra. de Ajalvir km. 4, E-28850 Torrejón de Ardoz, Madrid, Spain*
[7]*Departamento de Física, Ingeniería de Sistemas y Teoría de la Señal, Universidad de Alicante, E-03690 San Vicente del Raspeig, Alicante, Spain*
[8]*INAF – Osservatorio Astronomico di Padova, Vicolo dell'Osservatorio 5, Padova I-35122, Italy*
[9]*Department of Physics and Astronomy, University of Sheffield, Hicks Building, Hounsfield Road, Sheffield S3 7RH, UK*
[10]*Center for Astrophysics, Harvard-Smithsonian, 60 Garden Street, Cambridge, MA 02138, USA*
[11]*Anton Pannenkoek Institute for Astronomy, University of Amsterdam, NL-1090 GE Amsterdam, the Netherlands*
[12]*UK Astronomy Technology Centre, Royal Observatory Edinburgh, Blackford Hill, Edinburgh EH9 3HJ, UK*
[13]*Department of Physics and Astronomy, Johns Hopkins University, 3400 North Charles Street, Baltimore, MD 21218, USA*

Accepted 2020 October 18. Received 2020 September 28; in original form 2020 July 29

ABSTRACT

The presence of massive stars (MSs) in the region close to the Galactic Centre (GC) poses several questions about their origin. The harsh environment of the GC favours specific formation scenarios, each of which should imprint characteristic kinematic features on the MSs. We present a 2D kinematic analysis of MSs in a GC region surrounding Sgr A* based on high-precision proper motions obtained with the *Hubble Space Telescope*. Thanks to a careful data reduction, well-measured bright stars in our proper-motion catalogues have errors better than 0.5 mas yr^{-1}. We discuss the absolute motion of the MSs in the field and their motion relative to Sgr A*, the Arches, and the Quintuplet. For the majority of the MSs, we rule out any distance further than 3–4 kpc from Sgr A* using only kinematic arguments. If their membership to the GC is confirmed, most of the isolated MSs are likely not associated with either the Arches or Quintuplet clusters or Sgr A*. Only a few MSs have proper motions, suggesting that they are likely members of the Arches cluster, in agreement with previous spectroscopic results. Line-of-sight radial velocities and distances are required to shed further light on the origin of most of these massive objects. We also present an analysis of other fast-moving objects in the GC region, finding no clear excess of high-velocity escaping stars. We make our astro-photometric catalogues publicly available.

Key words: proper motions – stars: massive – Galaxy: centre – open clusters and associations: individual: Quintuplet – open clusters and associations: individual: Arches.

1 INTRODUCTION

At a distance of only 8 kpc (Gravity Collaboration 2019), the galactic centre (GC) region can be studied in exquisite detail, more than any other GC. The Central Cluster, the Arches, and the Quintuplet host rich massive-star (MS) populations; in addition to which there are at least 50 isolated MSs (see e.g. Cotera et al. 1996; Mauerhan et al. 2010a; Dong et al. 2011, 2015, and references therein), whose existence represents a conundrum for this environment (see e.g. Genzel, Eisenhauer & Gillessen 2010).

Most of these MSs (Dong et al. 2011) lie clearly outside of the two massive clusters and the central 20 pc region, dominated by the gravitational potential of the central black hole (see fig. 10 of Mauerhan et al. 2010a). The bulk of these stars is made up of Wolf–Rayet stars, very luminous OB supergiants or luminous blue variables that were discovered by virtue of their strong emission lines in the near-infrared (NIR) or strong X-ray emission (e.g. Mauerhan, Muno & Morris 2007; Mauerhan et al. 2009). Hence, MSs may only represent the tip of the iceberg since the weaker winds of lower mass OB stars make them more difficult to detect through the analysis of their spectral lines.

The origin of isolated MSs is currently unknown, but the unique GC environment favours some plausible formation scenarios. For example, some of these stars might be remnants of disrupted clusters, runaway stars (isolated OB-like objects with peculiar velocities greater than 30 km s^{-1}) ejected from the Arches or the Quintuplet or members of their tidal tails resulting from the interaction of the clusters with Sgr A* (e.g. Habibi, Stolte & Harfst 2014). Some of these isolated MSs might instead result from the disruption of binaries

★ E-mail: libra@stsci.edu

Table 1. List of observations used in this paper.

GO	Date	Instrument/camera	Filter	$N \times$ Exp. time
12915	Oct. 2012	WFC3/IR	F139M	108 × 300 s
				36 × 250 s
		ACS/WFC	F850LP	18 × 101 s
13771	Aug. 2015	WFC3/IR	F139M	108 × 300 s
				36 × 250 s
		ACS/WFC	F850LP	18 × 110 s

via interaction with the central black hole (the Hill mechanism; Hills 1988). This interaction would be responsible for the creation of hyper-velocity stars (HVSs). HVSs have velocities of thousands of km s^{-1}, which are greater than the Galactic escape velocity (Brown 2015), and would represent the extreme outliers in the velocity distribution of isolated MSs.

Some MSs have apparent lifetimes too short to justify their current positions had they been ejected from the nearest clusters or associations. It has been suggested that these stars might result from a peculiar mechanism of star formation such as the one in which single MSs form from small molecular clouds (Oey et al. 2004; Parker & Goodwin 2007; Lamb et al. 2010). This idea assumes the MSs to be normal single stars and not the product of more exotic systems (e.g. binary mergers of less massive but longer lived stars; de Mink et al. 2014; Renzo et al. 2019).

The proposed formation scenarios imprint distinct kinematic fingerprints on the MSs, so that studying the motion of MSs can help us understand how MSs have originated. Crowding and the complex spectra of these MSs make line-of-sight (LOS) radial-velocity measurements challenging. High-precision proper motions (PMs) can instead provide useful pieces of information about their 2D motions in the plane of the sky. State-of-art PMs over large field of views (FoVs) are nowadays provided by the *Gaia* Data Release 2 (DR2; Gaia Collaboration 2016, 2018a) catalogue. However, *Gaia* is ultimately blind towards the GC because of extinction, and its depth extends to a few kpc at most in the GC direction.

In this paper, we investigate the nature of MSs in the GC region by measuring their PMs with the *Hubble Space Telescope* (*HST*) optical and IR data. We also search for fast-moving stars in the region.

2 DATA SETS AND REDUCTION

The GC region was observed with the *HST*'s NIR channel of the Wide-Field Camera 3 (WFC3; pixel scale ∼130 mas $pixel^{-1}$) in 2012 October and 2015 August during programmes GO-12915 and GO-13771 (both PI: Lennon). The FoV was covered by 36 WFC3/IR pointings per epoch, each of which was observed with 4 images. Additional images were taken in parallel mode with the Wide-Field Channel (WFC; pixel scale ∼50 mas $pixel^{-1}$) of the Advanced Camera for Surveys (ACS). Parallel fields were covered by 18 ACS/WFC pointings of 1 image each. Table 1 lists all the observations. The FoV covered by the *HST* data is shown in Fig. 1.

We made use of `_flt`-type exposures (images bias-subtracted and flat-fielded but not resampled, produced by the official *HST* pipelines). ACS/WFC `_flt` images were also corrected for charge-transfer-efficiency (CTE) defects (Anderson & Bedin 2010).[1] For each camera/filter, we extracted positions and fluxes of isolated, bright sources in each image by fitting spatially variable point spread functions (PSFs). The PSFs for the ACS/WFC CCDs were tailored to each exposure starting from the publicly available *HST* library PSFs[2] as described in Bellini et al. (2017a). For WFC3/IR exposures, the publicly available library PSF models did not provide a satisfactory fit to the stellar profiles even after perturbation. In this case, we derived from scratch new, spatially variable PSF models using our data set, following the prescriptions given in Anderson (2016). These new models were then also perturbed on an image by image basis. Stellar positions were corrected for geometric distortion by means of the corrections available for *HST* WFC3/IR (Anderson 2016) and ACS/WFC detectors (Anderson & King 2006).[3]

Our data reduction is based on two photometric reductions. The first-pass photometry finds all detectable sources in a single wave of finding and measures them without considering the presence of close-by neighbours. This is a severe limitation in crowded regions like those towards the GC (see the top-right panel in Fig. 1). To overcome this issue, we performed a second-pass photometric reduction by means of the software `KS2`, a sophisticated `FORTRAN` routine currently used in the astro-photometric analyses of stellar clusters (e.g. Sabbi et al. 2016; Bellini et al. 2017b, 2018; Libralato et al. 2018b, 2019; Nardiello et al. 2018).

Starting from the outputs of the first-pass photometry, the second-pass photometry makes use of all the images at once to find all sources in the field. The combination of all the images enhances the detectability of faint sources otherwise lost in the noise of single exposures. Furthermore, the position and flux of each detected object are measured after all its neighbours are subtracted from the image.

In order to combine all the images of a given epoch/camera/filter, `KS2` requires the definition of a common astrometric and photometric reference system. We initially cross-identified well-measured, unsaturated, bright stars in our first-pass catalogues with the *Gaia*-DR2 catalogue by means of six-parameter linear transformations. The vast majority of *Gaia* stars within our FoV are Disc stars, which we used to define our reference-frame system. In total, we have about 3200 *Gaia* stars in our WFC3/IR field (with an average of 77 stars per image) and 2500 stars in our ACS/WFC field (with an average of 153 stars per image). The standard deviation of the positional residuals between a single WFC3/IR catalogue and the *Gaia* catalogue is, on average, 1.05 mas in the first epoch and 0.29 mas in the second epoch. For the ACS/WFC data, standard deviations of the positional residuals are 0.75 and 0.18 mas in the first and second epochs, respectively. The differences between the values in the first- and second-epoch data are mainly due to the Disc kinematics (GO-12915 data were obtained 2.7 yr before the *Gaia* DR2, while GO-13771 data were obtained at about the same epoch of the *Gaia* DR2). *Gaia* positions were projected on to a tangent plane centred at (R.A., Dec.) = (266.368 833, −28.920 167) deg (an arbitrary point in the centre of our FoV) and transformed from degrees to pixels adopting a pixel scale of 50 mas $pixel^{-1}$ (similar to that of the ACS/WFC detector). The *X*- and *Y*-axes were oriented towards west and north, respectively, and the reference tangent point was placed at position (14 500, 25 000). Then, master-frame positions were obtained by averaging the single-image positions once transformed into this *Gaia*-based reference system. Our master frames allow us to obtain an estimate of the positional precision we reached with our data. The median 1D positional rms for bright stars in the WFC3/IR data is of 1.5 mas in both epochs, while for bright objects in the ACS/WFC

[1]The WFC3/IR detector is not affected by CTE because of its different read-out mode with respect to that of charge-coupled devices.

[2]http://www.stsci.edu/∼jayander/STDPSFs/.
[3]http://www.stsci.edu/∼jayander/STDGDCs/.

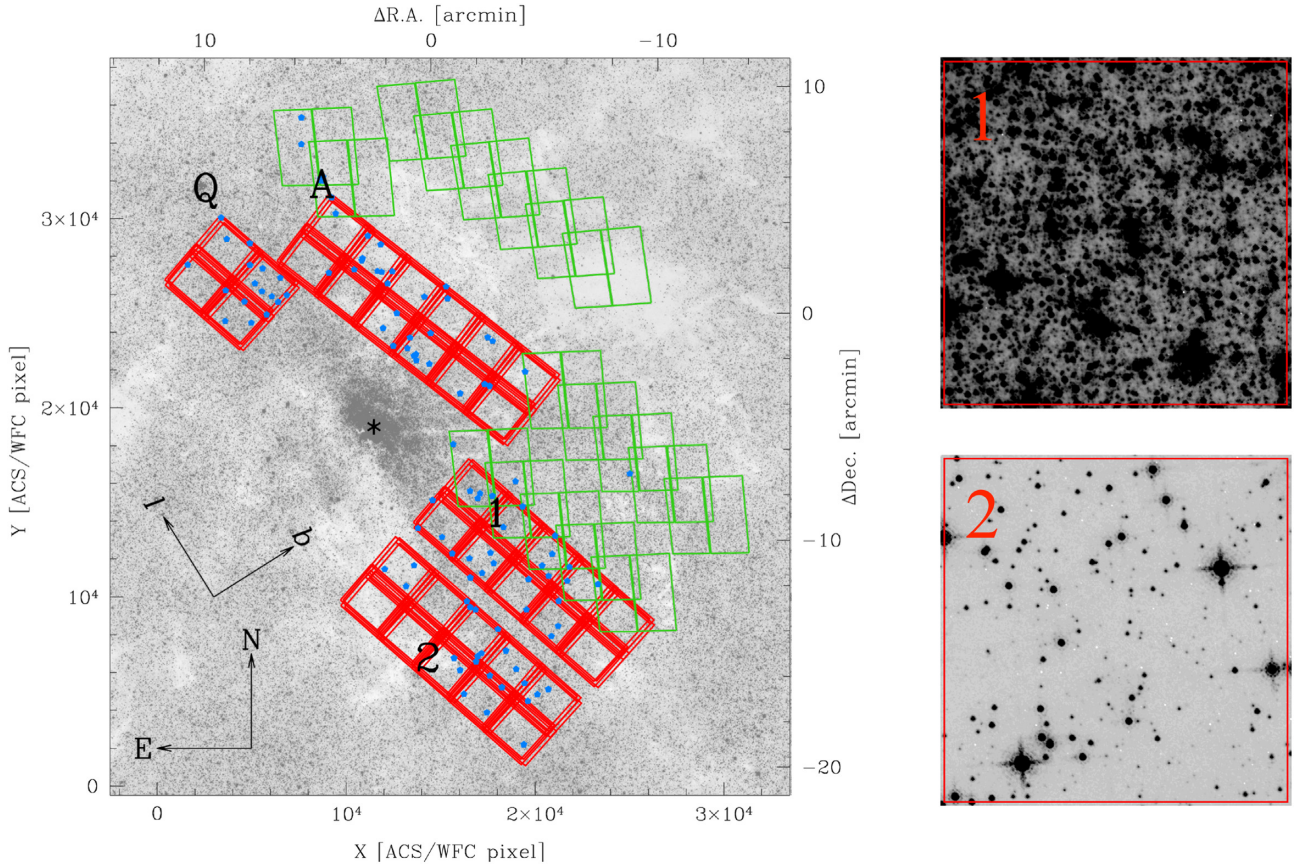

Figure 1. The FoV of the GO-12915+13771 data is shown in the left-hand panel (pixel scale 50 mas pixel^{-1}). The red and green outlines depict the footprints of the WFC3/IR and ACS/WFC data, respectively, and are overlaid to a K_S mosaic from the 'VISTA Variable in the Vía Láctea' survey (via ESO Science Portal). The black asterisk, 'Q', and 'A' mark the position of Sgr A*, the Quintuplet, and the Arches, respectively. Blue symbols highlight the targets of our investigation for which we derive a PM measurement. The right-hand panels show (with the same logarithmic scale) a zoom-in around typical low- (1) and high-extinction (2) regions in the WFC3/IR stacked image.

data with at least two measurements it is 1.2 mas in the first epoch and 1.3 mas in the second epoch.

The photometric registration of all the images into the same photometric system is not as straightforward as the astrometric set-up due to the non-contiguous FoV (see the left-hand panel of Fig. 1). Thus, we defined a common photometric system as follows:

(i) for each image, we measured the magnitude of bright, isolated objects on the corresponding WFC3/IR drizzle _drz or ACS/WFC _drc exposure using aperture photometry with a circular aperture with a five-pixel radius. We then transformed the PSF-based magnitudes to the aperture-based ones by applying the 2.5σ-clipped median offset found between the two systems. This normalizes the magnitude of each source in each image to a 1-s exposure (note that the WFC3/IR images are in electrons per second, so the magnitude difference is close to 0) and makes the photometric calibration straightforward in the later stage;

(ii) we combined (where possible) multiple _drz/_drc exposures on to a common reference-frame system. The magnitudes of the objects in the _drz/_drc master frame were computed by averaging the magnitudes of the stars in the single images once transformed on to the same reference system;

(iii) we cross-identified well-measured, bright stars in the zero-point-corrected first-pass catalogues defined in (i) with the _drz/_drc master frame defined in (ii), computed the residual zero-point differences, and corrected the first-pass photometry by these zero-point values. This last step ensures that any uncorrected photometric zero-point residual between different pointings is minimized;

(iv) the resulting corrected first-pass stellar magnitudes were then averaged together and defined the magnitudes of our master frame. The zero-point differences between the corrected first-pass stellar magnitudes and the master-frame magnitudes are lower than 0.01 mag on average and a few hundredth of a magnitude at most.

Once a common astro-photometric system has been defined for each epoch/camera/filter, we run KS2. KS2 measures stellar positions and fluxes using several different methods (see Bellini et al. 2017a, for details). In this work, we make use of the method based on PSF fitting of neighbour-subtracted stellar images, which is optimized for PM analyses (Bellini et al. 2018; Libralato et al. 2018b).

Finally, we transformed out KS2-based photometry on to the VEGA-mag flight system using the zero-points and infinite-aperture corrections provided by the STScI.[4]

In general, the higher the number of images mapping the same region of the sky, the more efficient is the KS2 detection of faint objects. However, KS2 is designed to search and fit an object within a radius of two pixels from the location of a local maximum on

[4]http://www.stsci.edu/hst/acs/analysis/zeropoints for ACS/WFC and http://www.stsci.edu/hst/instrumentation/wfc3/data-analysis/photometric-calibration/ir-photometric-calibration for WFC3/IR.

the reference frame found by combining all images. Sources that moved by more than two pixels in ∼2.8 yr (the temporal baseline between the GO-12915 and GO-13771 programs) in our data set are most likely to be missed by the KS2 finding algorithms if we use all the available data in a single run. Since the main goal of our project is to find fast-moving objects, we run KS2 for each epoch separately.

As described in Sabbi et al. (2016) and Bellini et al. (2017a), KS2 searches for and measures objects that satisfy various criteria (isolation, signal above the sky background, quality of the PSF fit, and total number of peaks in multiple images). The diagnostic parameters used to define these criteria do not have the same values in all images, but they change with, for example, the image quality (and the PSF), the value of the sky, and the level of crowding. We tested different combinations of these finding criteria and chose the parameters that gave us a good compromise between including real stars and excluding image artefacts or spurious detections. Thus, if the local values of the diagnostic parameters are very different from the global ones used to define KS2 searching criteria, KS2 could have missed real stars or included more spurious detections in the final list. In general, there are no one-size-fits-all parameters for such a large FoV. Our final photometric catalogues (one for each epoch) contain about 830 000 objects.

KS2 provides a series of diagnostic parameters that can be used to select a sample of well-measured objects (e.g. Libralato et al. 2018b). For the WFC3/IR catalogues, we define as well-measured stars those fulfilling all the following requirements: (a) Their quality of PSF fit (QFIT) parameter[5] is larger than the 85th percentile of the QFIT value at any given magnitude, but we additionally kept all objects with QFIT higher than 0.975 and rejected those with a QFIT lower than 0.6, regardless of their percentile value; (b) their magnitude rms is lower than the 85th percentile at any given magnitude (by analogy with the QFIT, sources with a magnitude rms lower/higher than 0.1/0.5 mag are also kept/discarded); (c) the ratio between the number of individual exposures actually used to measure position/flux of a given star and the total number of exposures in which the star was found is lower than 50 per cent; (d) their fraction of neighbour flux within the fitting radius with respect to the star flux before neighbour subtraction is less than 1; (e) the absolute value of their shape parameter RADXS (excess/deficiency of flux just outside of the fitting radius with respect to that expected from the PSF; see Bedin et al. 2008) is lower than the 85th percentile at any given magnitude (all sources with a RADXS lower than ±0.01 are considered as stellar-like objects, while detections with a RADXS larger than ±0.1 are significantly narrower/broader than the PSF expectation, and hence discarded); and (f) their flux within the PSF fitting radius is at least 3σ above the local sky. For the ACS/WFC catalogues, crowding is not an issue and bad-measured stars are clearly identified as outliers in the distributions of the diagnostic parameters mentioned above. At odd with the WFC3/IR case, to select well-measured stars we identified and removed by eye the outliers in the distribution of each diagnostic parameter. Finally, we combined the catalogues of the two runs of KS2 together and kept only objects that were measured in both epochs.

KS2 also outputs single exposure catalogues containing raw position and flux of each detected source. These positions and fluxes are superior over those obtained with the first-pass photometry stage, since KS2 measurements are deblended. Hereafter, we will refer to these KS2-based catalogues simply as *raw* catalogues.

[5]The QFIT parameter is a linear-correlation coefficient between the pixel values in the image and those of predicted by the PSF. A well-measured star has a QFIT close to unity.

2.1 Ancillary catalogues

Most of the stars in our FoV are observed with only one filter in our *HST* data. In order to build colour–magnitude diagrams (CMDs) for the subsequent analyses, we linked our photometric catalogues to other catalogues from previous or ongoing surveys of the GC:

(i) the catalogue of Dong et al. (2011), made as part of the Paschen α survey of the GC with the *HST* Near-Infrared Camera and Multi-Object Spectrometer (NICMOS; Wang et al. 2010), provides F187N- and F190N-filter photometry;

(ii) the 'GALACTICNUCLEUS' JHK_S catalogue of Nogueras-Lara et al. (2019), obtained with HAWK-I@VLT (Very Large Telescope) speckle data;

(iii) the PSF-based catalogue of Surot et al. (2019), made with the 'VISTA Variable in the Vía Láctea' (VVV) data.

Depth and completeness of these catalogues are heterogeneous.

The HAWK-I@VLT instrument has a higher angular resolution than that of the VIRCAM@VISTA imager (106 mas pixel^{-1} versus 339 mas pixel^{-1}), which is an advantage in crowded environments such as the region close to the GC. For this reason, we chose to rely mainly on the GALACTICNUCLEUS JHK_S catalogue. However, while this catalogue completely covers our WFC3/IR data, it only partially overlaps with our ACS/WFC data. As such, we used the VVV data to study the ACS/WFC region. We found magnitude zero-point differences between the GALACTICNUCLEUS and the VVV photometry. We corrected the VVV photometry to match that of the GALACTICNUCLEUS catalogue by linearly interpolating the median magnitude difference between the two catalogues in different 0.5-mag bins. The zero-point corrections between the VVV and GALACTICNUCLEUS photometry are of the order of 0.1–0.2 mag in the J filter and 0.4–0.6 mag in the K_S filter.

As for the GALACTICNUCLEUS catalogue, the Paschen α data cover the entire WFC3/IR area and only part of the ACS/WFC region. The Paschen α catalogue also contains a list of MSs in the GC region.

3 PROPER MOTIONS

State-of-the-art techniques currently used to study the internal kinematics of globular clusters with *HST* (e.g. Bellini et al. 2014) are based on the selection of a reference population of stars. Cluster stars are typically chosen as a reference because, to first order, they are moving towards the same direction on the sky and have a tight distribution in the vector-point diagram (VPD). However, this method is not easy to apply to our project. The different stellar populations in the field have complex PM distributions in the VPD as a result of the Galactic kinematics and the reflex motion of the Sun. The uneven dust distribution towards the GC (e.g. the right-hand panels of Fig. 1) adds further complications. For example, highly reddened regions only leave nearby objects visible, while regions with a less severe reddening contain a mix of stars at different distances out to beyond the GC. The combined effect of kinematics and dust distribution could bias our PMs if we select reference samples with different bulk PMs across the FoV. For this reason, PMs are computed in a different fashion, by taking advantage of the *Gaia*-DR2 catalogue (for a similar technique, see also Bedin & Fontanive 2018). We computed two, independent sets of PMs, one using only WFC3/IR data and one using only ACS/WFC data, so as to minimize mismatches between images taken using significantly

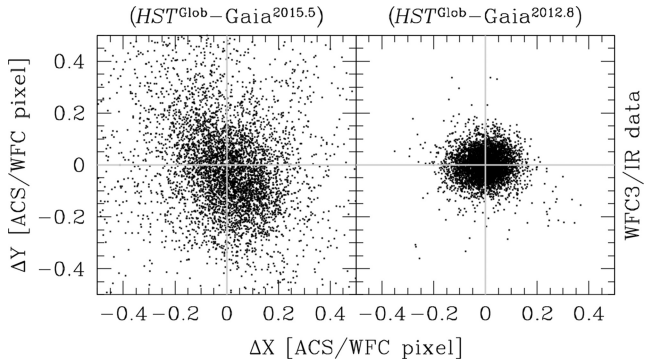

Figure 2. Example of positional residuals between the 2012.8 WFC3/IR positions (HST^{Glob}) and the *Gaia*-DR2 positions at epoch 2015.5 (left-hand panel) and at epoch 2012.8 (right-hand panel). Six-parameter, global linear transformations were used to transform the stellar positions between the reference systems. Displacements are in units of ACS/WFC pixels.

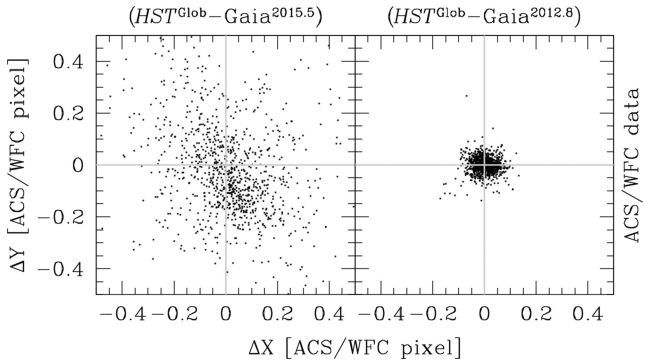

Figure 3. As in Fig. 2, but for the ACS/WFC data.

different bandpasses, but at the unavoidable expense of having fewer images at our disposal in the overlapping regions between the two data sets. In Appendix B, we provide comparisons of independent PM measurements in the overlapping regions as a sanity check.

For each of the two data sets, we defined an absolute reference system using the *Gaia*-DR2 catalogue as follows. First, we projected the *Gaia*-DR2 catalogue as described in Section 2. We used equation (2) of Gaia Collaboration (2018b) to define an orthographic projection of the *Gaia*-DR2 PMs into Equatorial coordinates. Then, we used *Gaia*-DR2 PMs to predict the position of each source in the *Gaia* catalogue at the average epochs of the GO-12915 (2012.8) and GO-13771 (2015.6) data sets, respectively. We removed from the *Gaia* sample all objects that (i) are fainter than $G = 19$, (ii) have a PM error in either coordinate larger than 0.6 mas yr^{-1}, or (iii) do not fulfil the requirement described by equation (C.1) of Lindegren et al. (2018).

For each star in the catalogue, we used six-parameter, global linear transformations to transform its position on to the *Gaia*-DR2 reference system of the corresponding epoch (hereafter, we refer to these positions as transformed positions). In addition, we also produced a set of transformed positions by applying a local adjustment in order to mitigate the possible presence of small, uncorrected systematic residuals in, e.g. the *HST* PSF models and the geometric-distortion solution. This adjustment (the so-called 'boresight' correction described in Anderson & van der Marel 2010) is defined as the average of the positional residuals between the transformed *HST* positions and the *Gaia*-DR2 positions of the closest N stars to the target. These local corrections are based on the closest $N = 24$ (for the WFC3/IR data) or $N = 25$ (for the ACS/WFC data) sources to each object.[6] The median distance of the furthest reference star in a WFC3/IR image is about 750 WFC3/IR pixels (∼90 arcsec), while in an ACS/WFC image it is about 2200 ACS/WFC pixels (∼110 arcsec).

Figs 2 and 3 show the impact of the stellar PMs on the distribution of positional residuals between *HST* and *Gaia*. In the left-hand panels, we show the positional residuals between the 2012.8 *HST* positions and the *Gaia*-DR2 positions at the reference epoch of the *Gaia*-DR2 catalogue (2015.5). In the right-hand panels, we show the positional residuals of the same stars after *Gaia*-DR2 positions are moved at the epoch of *HST* observations. A tight distribution of the positional residuals is a proxy of accurate transformation between the frames. The distributions of the positional residuals in the right-hand panels clearly show how important it is to take into account stellar motions even at this initial cross-matching stage. The comparison of the positional residuals between the 2015.6 *HST* positions and the *Gaia*-DR2 positions with and without moving the *Gaia*-DR2 positions at the epoch of *HST* observations shows negligible differences, as expected.

Global transformations proved to be superior (tighter distribution of positional residuals) for the WFC3/IR data, while the opposite applies to the ACS/WFC data. This is probably related to the available number of stars in common between *Gaia* and *HST* catalogues. In general, there are plenty of common stars in the ACS images that can be used to derive the boresight correction, which makes the local adjustment effective. On the other hand, there are not many stars that are unsaturated and well measured in both the *Gaia* and WFC3 data: Much larger searching radii are typically needed for the WFC3 data to find the closest 24 stars for the boresight correction, resulting in negligible improvements over the global transformations alone. For this reason, we chose to use the globally transformed positions for the WFC3/IR-based PMs and the locally corrected positions for the ACS/WFC-based PMs. Finally, it should be highlighted that the positional residuals have a larger dispersion along the X-axis. The X- and Y-axes are aligned and oriented as −R.A. and +Dec. by construction. In this GC field, *Gaia* positional and PM errors are larger along the R.A. than the Dec. direction because of the scanning pattern of the satellite, and are the probable cause of this feature.

The final single-epoch position of a star is computed as the robust average of the transformed positions of all images at the epoch. An outlier-rejection step was performed with a jackknife resampling technique similarly to what is described in Bellini et al. (2014).

After these steps, we had two catalogues, one for each epoch of our data. The positions of the objects in these two catalogues are in the same absolute reference system defined by the *Gaia*-DR2 catalogue, only at different epochs. Therefore, our absolute PMs can be simply defined as the difference between the positions in the two epochs, divided by the average temporal baseline. The PM errors were obtained by adding in quadrature the positional errors in each epoch and dividing by the temporal baseline.

The main features and caveats of our PM catalogue are the following:

(i) our PMs are absolute, not relative;

[6]The number of reference stars used to calculate these local corrections was empirically chosen as the largest value that allowed us to obtain a PM measurement for all stars across the FoV, even in regions covered by only one image per epoch.

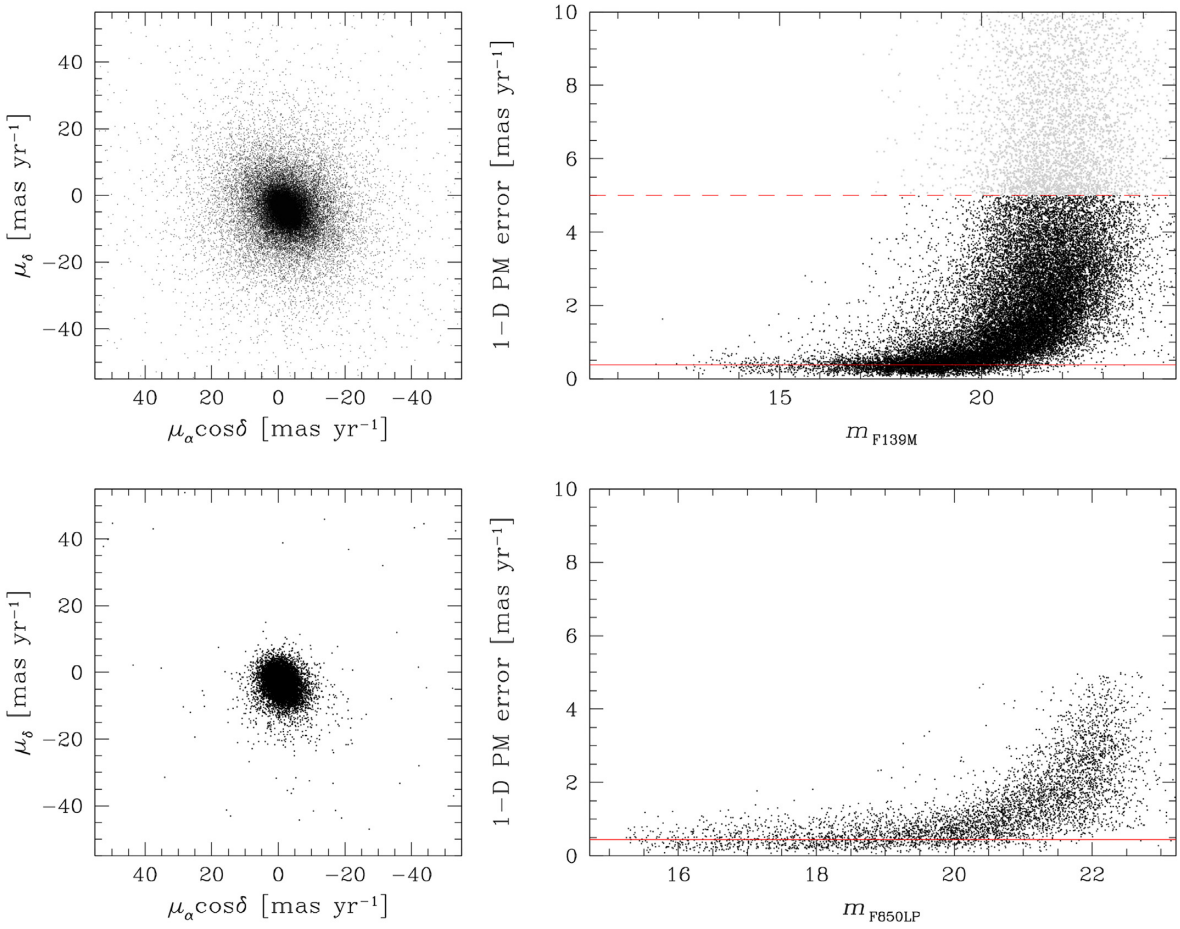

Figure 4. Top panels: the VPD (left) and the 1D PM error as a function of the $m_{\rm F139M}$ magnitude (right) for the WFC3/IR-based PMs. In the right-hand panel, the red, solid horizontal line is set at the median value of the PM errors for bright stars (0.38 mas yr^{-1}). Grey points are stars with a PM error larger than a threshold set at 5 mas yr^{-1} (red, dashed horizontal line; see the text for details). These stars are not considered in our analysis. Only 5 per cent of the points are shown in each panel for clarity. Bottom panel: the VPD and the 1-D PM error versus $m_{\rm F850LP}$ magnitude for the ACS/WFC-based PMs. The median PM error for bright stars is 0.45 mas yr^{-1} (red, solid horizontal line).

(ii) any systematic error in the *Gaia*-DR2 catalogue is also present in our catalogue;

(iii) crowding and detector cosmetics facilitate mismatches between the catalogues, especially at faint magnitudes where the signal-to-noise ratio is low. Fast-moving objects should be carefully checked. In our analysis, we exclude all objects that moved by more than 5 pixels in 2.86 yr, i.e. have a PM greater than about 70 mas yr^{-1}. At the distance of Sgr A*, this value corresponds to ∼2600 km s^{-1}. We chose this threshold as a compromise between removing mismatches in our catalogue and keeping potential HVSs;

(iv) the median PM error of bright stars in the WFC3/IR-based PM catalogue is 0.38 mas yr^{-1}, while in the ACS/WFC-based PM catalogue it is 0.45 mas yr^{-1} (see Fig. 4);

(v) stars measured in only one exposure in an epoch do not have positional errors for that epoch. For them, the catalogue lists a flag value of 99.99 mas yr^{-1} for their PM error. These stars were included in the analyses of MSs and fast-moving objects.

(vi) the positional error of stars measured in only two exposures in an epoch is defined as the absolute difference between the two values divided by $\sqrt{2}$. Therefore, their corresponding PM errors are likely underestimated.

Fig. 4 shows VPD (left-hand panels) and PM error as a function of magnitude (right-hand panels) for stars in the WFC3/IR (top) and ACS/WFC (bottom) PM catalogues. The red, solid, horizontal lines in the right-hand panels are set at the median PM error of bright stars. In the following analysis, we considered as well-measured stars those with a PM error lower than the 85th percentile of the error distribution at any given magnitude for the WFC3/IR-based PMs and lower than a threshold drew by hand for the ACS/WFC-based PMs. In the WFC3/IR PM catalogue, we also kept all objects with a PM error lower than 0.7 mas yr^{-1} (i.e. about twice the median PM error of bright, well-measured stars) and discarded those with a PM error larger than 5 mas yr^{-1} (red, dashed horizontal line in the top-right panel of Fig. 4) in addition to the percentile-based selection on the PM error. No upper limit was set to the PMs derived from the ACS/WFC data because of the higher astrometric quality.

Appendix A presents an in-depth comparison between our *HST* and *Gaia*-DR2 PMs. While there is general agreement, we find position-dependent systematics across the FoV, in particular in the outer regions near the edge. Stars brighter than $G \sim 18$ do not present significant colour- and magnitude-dependent systematic errors. The lower astrometric quality of the *Gaia*-DR2 PMs for fainter stars is likely the main cause of the systematic trends visible in Figs A3 and A4.

The comparison between the WFC3/IR- and ACS/WFC-based PMs is shown in Appendix B. There is a difference between the

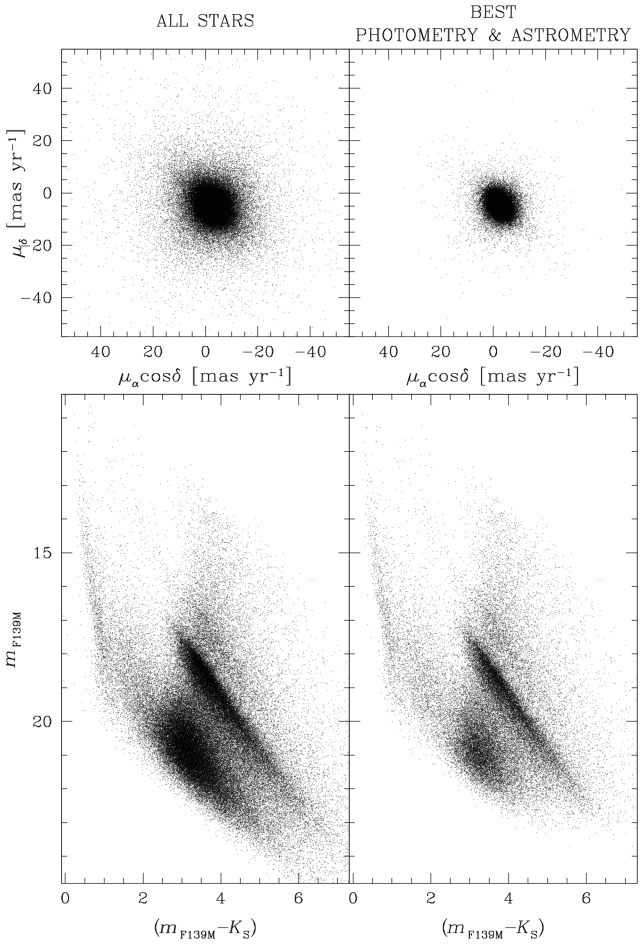

Figure 5. In the left-hand panels, we show the VPD (top) and the m_{F139M} versus $(m_{F139M} - K_S)$ CMD (bottom) with all stars with a WFC3/IR-based PM and a K_S magnitude measurement. In the right-hand panels, we show only stars that passed all photometric and astrometric selection criteria. Only 25 per cent of the stars are shown for clarity.

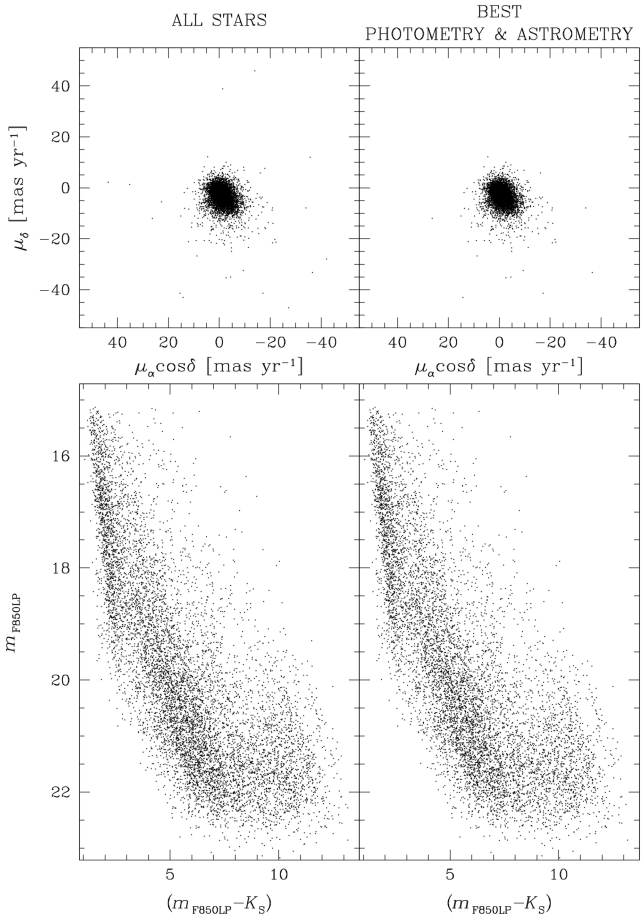

Figure 6. Similar to Fig. 5, but for the ACS/WFC data.

ACS/WFC and WFC3/IR PMs along the R.A. direction. However, this systematic difference disappears if we consider relatively isolated stars in the WFC3/IR data. Crowding is therefore an important contributor of systematic errors, particularly for faint stars. Our PM catalogues are made publicly available (Appendix C). All the aforementioned caveats and the quality checks in Appendixes A and B should be considered when using these PM catalogues.

The left-hand panels of Fig. 5 show the VPD and the m_{F139M} versus $(m_{F139M} - K_S)$ CMD for all stars in common between our WFC3/IR and the GALACTICNUCLEUS catalogues, while those on the right present similar plots just for well-measured stars. It is worth noticing the X-shaped trails of larger PM stars in the VPD, which is aligned with the *X*/*Y*-axes of the detector (see the orientation of the WFC3/IR data in Fig. 1). We found that the X-shaped trails are more noticeable the fainter the stars. Recently, Plazas et al. (2018, and references therein) report and analyse the so-called 'brighter-fatter' effect in the WFC3/IR data, which causes charge redistribution among the pixels. The investigation of this effect is out of the scope of our paper, but the magnitude dependence and the *X*/*Y* orientation of the effect we see in the VPDs seem to suggest a relation with the 'brighter-fatter' effect.

VPDs and m_{F850LP} versus $(m_{F850LP} - K_S)$ CMDs for stars in common between our ACS/WFC and the VVV catalogues are presented in Fig. 6. Optical data are basically blind to most of the Bulge population, and the vast majority of the stars measured in the ACS/WFC data are Disc stars.

4 A KINEMATIC VIEW OF THE GC REGION

In this section, we provide a brief description of the astronomical scene in our field. In the following, we consider only well-measured stars that passed all photometric and astrometric quality selections, unless declared otherwise. In this and the following sections, all figures related to WFC3/IR-based PMs show only a fraction of the stars in the field, for clarity.

4.1 IR view

Various populations can be distinguished along the LOS towards the GC. We use the CMDs shown in Fig. 7 to disentangle them. The CMDs immediately reveal the presence of a narrow bluer sequence (hereafter, the blue sequence) and a broader redder sequence (hereafter, the red sequence).

Stars in common with the *Gaia*-DR2 catalogue are shown as blue open circles. These objects are mainly located along the blue sequence and have a median parallax of ∼0.5 mas (∼2 kpc), i.e. they are Disc stars. The majority of the stars in the CMDs are instead part of the red sequence. The broadening of the red sequence is a

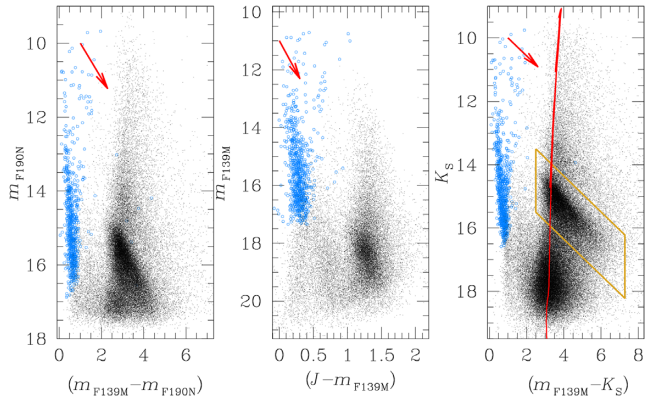

Figure 7. CMDs based on the WFC3/IR data. Left-hand panel: m_{F190N} versus $(m_{F139M} - m_{F190N})$ CMD. Middle panel: m_{F139M} versus $(J - m_{F139M})$ CMD. Right-hand panel: K_S versus $(m_{F139M} - K_S)$ CMD. Blue open circles depict stars in common with the *Gaia*-DR2 catalogue. In each CMD, the direction of the reddening vector is indicated by a red arrow. The reddening vector is computed by assuming an arbitrary extinction A_{F139M} in each plot and the extinction index $\alpha = 2.3$ of Nogueras-Lara et al. (2018). A PARSEC isochrone for 10-Gyr-old stars with [Fe/H] $= -0.16$ at 8.2 kpc from the Sun representing the Bulge population is fitted by eye as reference in the rightmost panel. The gold rectangle marks the location of the Bulge red clump.

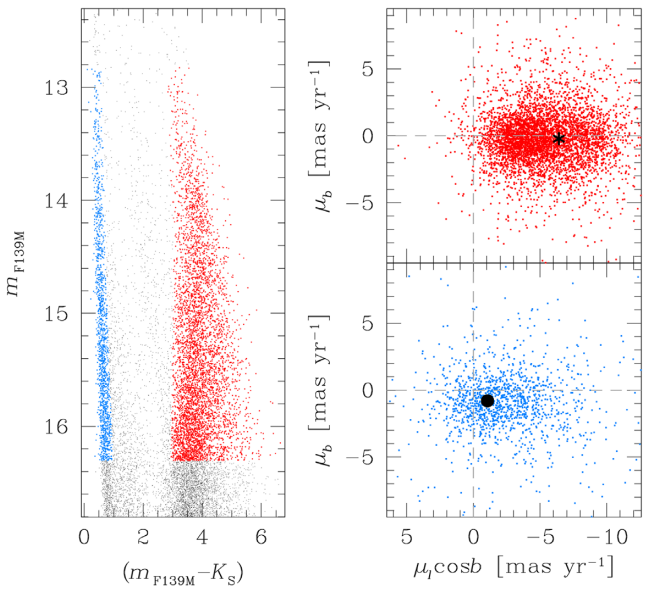

Figure 8. The left-hand panel presents the m_{F139M} versus $(m_{F139M} - K_S)$ CMD of the stars in our WFC3/IR-based PM catalogue. Disc stars are shown as blue points, while Bulge/Bar objects are depicted in red. The corresponding VPDs of the PMs in Galactic coordinates are shown in the right-hand panels. The grey, dashed lines are set at $\mu_l \cos b = 0$ mas yr^{-1} and $\mu_b = 0$ mas yr^{-1}. The black dot in the bottom-right VPD represents the expected PM of Disc stars at 2 kpc from the Sun, while the star on the top-right VPD is the PM of Sgr A* (see Table 2).

proxy of the severe extinction that affects these stars and suggests that these stars are Bulge/Bar objects within a few kpc from the GC. As a reference, we plot in the rightmost panel a 10-Gyr-old PARSEC isochrone (Bressan et al. 2012) with [Fe/H] $= -0.16$ (e.g. Rich et al. 2017) and with a distance of 8.2 kpc from the Sun, to represent an old stellar population in the Bulge of the Galaxy. Finally, sources between the blue and red sequences are an admixture of Disc stars further than ∼2 kpc from the Sun and Bulge/Bar objects with a less-severe extinction (plus the scatter due to the photometric errors).

We can reach the same conclusions with astrometric arguments. In the left-hand panel of Fig. 8, we selected a sample of bright stars along the Disc (in blue) and Bulge/Bar (in red) sequences in the CMD. The VPDs in Galactic coordinates[7] in the right-hand panel of Fig. 8 demonstrate that our PMs are accurate enough to detect the different motions of the two populations.

We know from the *Gaia*-DR2 catalogue that these Disc stars are, on average, at a distance of a few kpc from the Sun. According to the recent work of Reid et al. (2019), the rotation velocity of the Galaxy at the distance of these stars is ∼237 km s^{-1}. By assuming from the same paper the rotation velocity for the Sun of ∼247 km s^{-1}, this means that the Disc stars in the blue sequence of the CMD should have an apparent motion along the Galactic longitude l of about −10 km s^{-1}, i.e. −1.05 mas yr^{-1}. The Sun also has a motion of +7.6 km s^{-1} perpendicular to the plane of the Galaxy. If we assume that our Disc stars have a negligible vertical motion, the expected apparent motion along the Galactic latitude b of the Disc stars at 2 kpc should be of −7.6 km s^{-1}, i.e. −0.8 mas yr^{-1}. In the bottom-right VPD in Fig. 8, we plot as a black dot the expected apparent PM of Disc stars. The good agreement between the expected motion of Disc stars in our FoV and the PMs of blue-sequence stars supports the idea that these objects are within a few kpc from the Sun.

Stars belonging to the red sequence have a PM distribution different from those of the Disc stars (Fig. 8). The black star in the top-right VPD marks the absolute PM of Sgr A* from Reid & Brunthaler (2020). Again, red-sequence stars have PMs similar to that of Sgr A*, thus suggesting they are part of the same GC region. Interestingly, the VPD of Bulge/Bar stars highlights the presence of two different groups of stars, whose distributions are mainly elongated along the l direction.

To better understand the nature of the two stellar groups in the GC region, we extended the sample to fainter stars for a better statistics, made a histogram (with a bin width of 0.25 mas yr^{-1}) of the PMs along the $l\cos b$ direction, and fit the histogram with a dual Gaussian function (top-left panel of Fig. 9). We found a tighter group (green contour) centred at $\mu_l \cos b \sim -3.6$ mas yr^{-1}, and a broader group (yellow contour) centred at $\mu_l \cos b \sim -7.5$ mas yr^{-1}. The mean PM of the former group is (just) a few mas yr^{-1} (∼100 km s^{-1} at the distance of Sgr A*) larger than that of Sgr A* and might contain stars in front of the GC. The latter group has a PM similar to that of Sgr A*, and it might represent stars at the distance of Sgr A*. The m_{F139M} versus $(m_{F139M} - K_S)$ CMD of these two groups of stars (right-hand panel) shows that stars with a PM similar to that of Sgr A* are fainter, suggesting they are further from the Sun than the other group. Yellow points are also redder than green dots, suggesting that the uneven dust distribution in the field could also cause the magnitude–colour difference shown in the CMD. However, the direction of the reddening vector does not seem consistent with the direction of the colour/magnitude offset between yellow and green points, which means that extinction alone cannot explain the observed offset in the CMD.

[7]In this paper, Galactic PM errors are computed following a Monte Carlo approach similar to that described in Libralato et al. (2020). For each star, we used 10 000 samples of its Equatorial PM. These samples were drawn by a Gaussian distribution with average and σ equal to the absolute PM and errors of the star. Then, we converted the PMs of these samples from the Equatorial to the Galactic reference system. Finally, we defined as the Galactic PM error of the star the standard deviation of the obtained distributions.

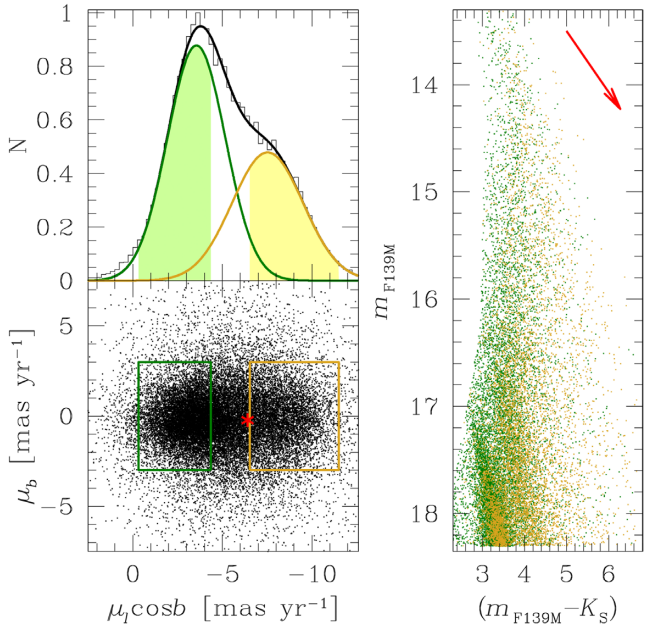

Figure 9. Top-left panel: histogram of the $\mu_l \cos b$ PMs of bright, well-measured Bulge/Bar stars. The dual Gaussian fit to the histogram is shown with a black line, while the individual Gaussian components are shown in green and yellow. We used these Gaussian functions to select two samples of stars for each group (shaded pale green and yellow regions). To avoid contamination between the two groups, we selected only stars from 0.5σ to 2σ from the peaks of the Gaussian functions. Bottom-left panel: VPD of the absolute PMs in Galactic coordinates. The red asterisk marks the PM of Sgr A*. Right-hand panel: m_{F139M} versus ($m_{F139M} - K_S$) CMD. Only stars enclosed in the green and yellow rectangles are shown in the CMD and are colour coded accordingly. The red arrow represents the reddening vector.

To verify that distance from the GC is the main factor in explaining the kinematic and photometric differences between the two groups of stars, we performed a simple test. We selected five regions from the stacked image with high stellar densities, i.e. with low extinction (as in panel 1 of Fig. 1), and five heavily absorbed regions (as those in panel 2 of Fig. 1). Regions with high extinction should contain mainly stars closer to us, while regions with low extinction should present a mix of stars at different distances, up to the GC and possibly beyond. In Fig. 10, we plot the CMDs for the stars in each region. Then we selected red-clump stars in both CMDs. In the top panels, we show the corresponding histograms (bin width of 0.25 mas yr^{-1}) of the PMs along the $l\cos b$ direction. The 'high-extinction' histogram shows a clear drop of stars with $\mu_l \cos b \lesssim -6$ mas yr^{-1} with respect to the 'low-extinction' histogram, as expected if objects with $\mu_l \cos b \lesssim -6$ mas yr^{-1} are those closer to (in front or behind) the GC.

4.2 Optical view

Fig. 11 presents an overview of CMDs made with the ACS/WFC data. Most of the stars are close-by Disc stars, but some bright Bulge/Bar objects seem still present. However, the interpretation of the different features visible in these CMDs is not straightforward in these colour combinations with the F850LP filter.

In the left-hand panel of Fig. 12, we plot the K_S versus ($J - K_S$) CMD for the stars in the ACS/WFC data for which we have PM measurements. We selected a sample of stars in the Disc sequence and one in the brightest end of the redder sequence of the CMD. The right-hand panels of Fig. 12 present the VPDs of the PMs of the blue

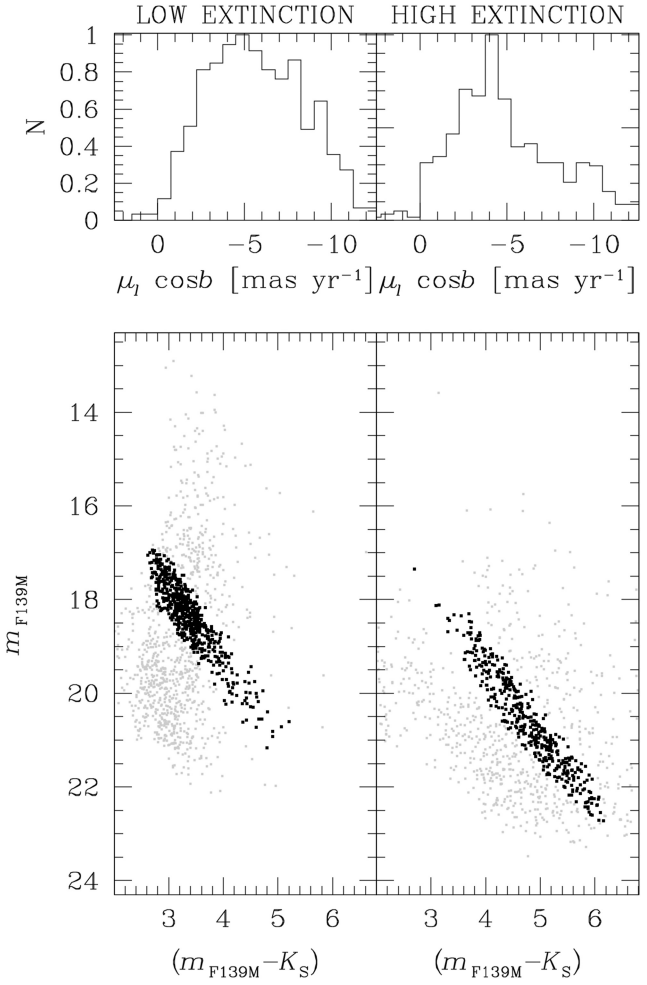

Figure 10. Top panels present the histograms of $\mu_l \cos b$ for red-clump stars in low- (left) and high-extinction (right) regions. The corresponding m_{F139M} versus ($m_{F139M} - K_S$) CMDs for stars in the two regions are shown in the bottom panels. Black points are red-clump stars, while the other grey points represent all other Bulge/Bar stars in these regions.

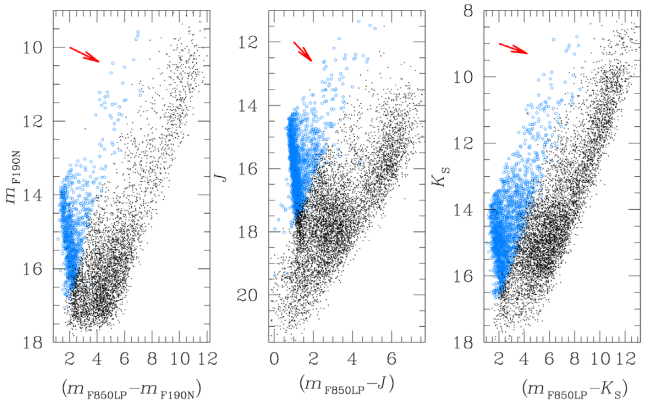

Figure 11. CMDs based on the ACS/WFC data. Left-hand panel: m_{F190N} versus ($m_{F850LP} - m_{F190N}$) CMD. Middle panel: J versus ($m_{F850LP} - J$) CMD. Right-hand panel: K_S versus ($m_{F850LP} - K_S$) CMD. As in Fig. 7, stars in common with the *Gaia*-DR2 catalogue are shown as blue open circles. The red arrows represent the direction of the reddening vector and it was computed by assuming an arbitrary extinction $A_{F850LP} = 2.5$ in each plot and the extinction index $\alpha = 2.3$ of Nogueras-Lara et al. (2018).

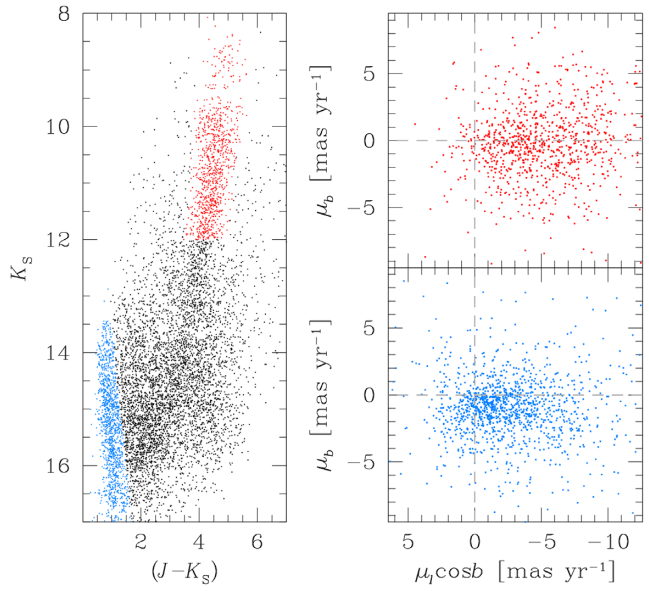

Figure 12. The K_S versus $(J - K_S)$ CMD of the stars in the ACS/WFC data for which we have a PM measurement is shown in the left-hand panel. Blue and red points highlight a sample of Disc objects and a group of Bulge/Bar stars. The right-hand panels present the VPDs of the PMs in Galactic coordinates for the Bulge/Bar (top panel) and Disc (bottom panel) stars.

and red stars. As in Fig. 8, their PMs show the different kinematics of these stars.

Bulge/Bar stars in the GC region are faint in the F850LP filter and the only stars in common between the ACS/WFC data and the VVV catalogue are probably bright stars in front of the GC, closer to the Sun than those visible in the WFC3/IR FoV. Fig. 13 shows the K_S versus $(J - K_S)$ CMD of stars in the WFC3/IR FoV (black points) and in the ACS/WFC data (red, open circles). Stars with $(J - K_S) \lesssim 4$ are present in both the WFC3/IR and ACS/WFC data. Stars redder than $(J - K_S) \sim 4$ in common between the WFC3/IR and ACS/WFC catalogues are only those in the bright blue side of Bulge/Bar sequence, as expected if Bulge/Bar stars in ACS/WFC field are closer and less reddened than those in the WFC3/IR data.

4.2.1 *The Arches cluster*

Recently, Libralato et al. (2020) linked the PM catalogue of Stolte et al. (2015) to an absolute system by means of the *Gaia*-DR2 catalogue, and measured the absolute PM of the Arches as:

$$(\mu_\alpha \cos\delta, \mu_\delta)^{\mathrm{Arches-}L20} = (-1.45 \pm 0.23, -2.68 \pm 0.14)\,\mathrm{mas\ yr^{-1}}. \quad (1)$$

The Arches cluster is present in the north-east region of the FoV and it is covered by two ACS/WFC images per epoch. As an independent check of our PMs, we computed the absolute PM of the Arches using our *HST*-based PMs and compared this new estimate with that of Libralato et al. (2020).

Most of Arches' members are not detected by KS2 because they are either too faint or did not pass the detection criteria of KS2 (see the discussion in Section 2). Clark et al. (2018) identified MSs' likely members of the Arches cluster according to their LOS velocities. Some of these MSs are also present in our catalogue (see the later discussion in Section 5). The average PM of these MSs measured in two images per epoch, which represents an estimate of the absolute PM of the Arches, is

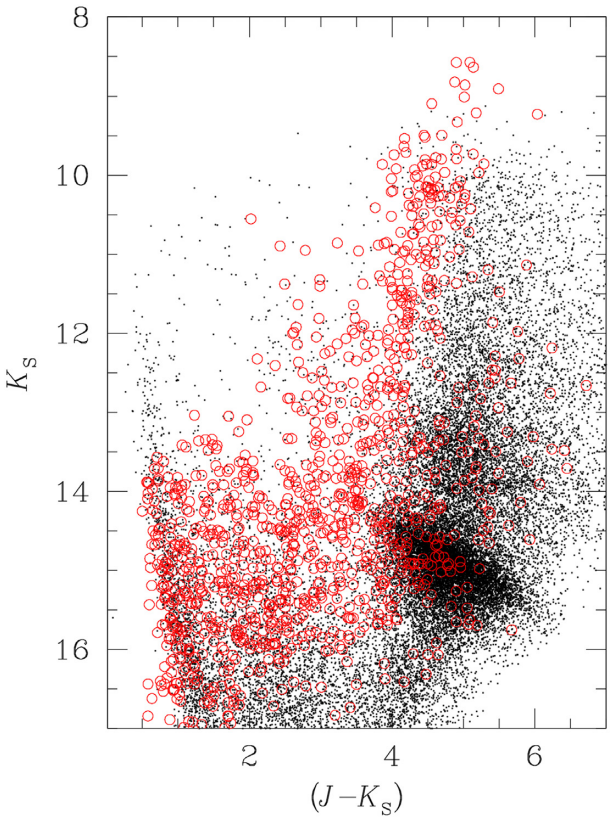

Figure 13. The K_S versus $(J - K_S)$ CMD of the stars in the WFC3/IR data (black points) and in the ACS/WFC data (red, open circles).

$$(\mu_\alpha \cos\delta, \mu_\delta)^{\mathrm{Arches-This\ work\ (1)}} = (-1.24 \pm 0.78, -2.44 \pm 0.68)\,\mathrm{mas\ yr^{-1}}. \quad (2)$$

This value is in agreement with the estimate of Libralato et al. (2020) at the 1σ level, although our PM errors are larger because of the faintness (i.e. less-precise PMs) of our reference objects.

We also took advantage of Disc stars in our ACS/WFC PM catalogue and converted the PMs of Stolte et al. (2015) from relative to absolute values following the prescription of Libralato et al. (2020). Our second independent estimate of the absolute PM of the Arches is

$$(\mu_\alpha \cos\delta, \mu_\delta)^{\mathrm{Arches-This\ work\ (2)}} = (-1.34 \pm 0.41, -2.11 \pm 0.20)\,\mathrm{mas\ yr^{-1}}. \quad (3)$$

The agreement with the estimate of Libralato et al. (2020) is at the $\sim 2\sigma$ level. The average PM error of the *Gaia* stars used in the work of Libralato et al. (2020) for the relative-to-absolute conversion is about 0.43 mas yr^{-1}, while that of the stars in our PM catalogue used for the same task is 0.76 mas yr^{-1}. Therefore, we chose to keep the original PM estimate of Libralato et al. (2020) as the absolute PM of the Arches in the rest of the paper.

5 KINEMATICS OF MASSIVE STARS

Most MSs in our field were identified by Dong et al. (2011) as part of the NICMOS survey of Wang et al. (2010). Dong et al. (2011) found several Paschen α-emitting candidates, most of which are evolved MSs with strong winds. The authors released a list of 152

Table 2. Position and PMs of Sgr A*, the Arches, and the Quintuplet.

Object	R.A. (deg)	Dec. (deg)	$(\mu_\alpha \cos\delta, \mu_\delta)$ (mas yr^{-1})	$(\mu_l \cos b, \mu_b)$ (mas yr^{-1})
Sgr A*	266.416 8371	− 29.007 810 56	$(-3.156 \pm 0.006, -5.585 \pm 0.010)$	$(-6.411 \pm 0.008, -0.219 \pm 0.007)$
Arches	266.4604	− 28.8244	$(-1.45 \pm 0.23, -2.68 \pm 0.14)$	$(-3.05 \pm 0.17, -0.16 \pm 0.20)$
Quintuplet	266.5578	− 28.8300	$(-1.19 \pm 0.09, -2.66 \pm 0.18)$	$(-2.89 \pm 0.16, -0.38 \pm 0.12)$

Note. (i) Position and PMs of Sgr A* are from Reid & Brunthaler (2020). (ii) Positions of the Arches and Quintuplet clusters are from the SIMBAD data base, while PMs are from Libralato et al. (2020).

confirmed Paschen α emitters (hereafter Primary list) and a list of 189 potential candidates for which it was not possible to perform a clear classification (Secondary list).

We also included MSs from Clark et al. (in preparation). Recently, Clark et al. (in preparation) undertook a NIR spectroscopic survey of the Arches, Quintuplet, and diffuse MS population in the GC region using SINFONI and KMOS on the European Southern Observatory (ESO) VLT. The list of their targets comprises two subsets. The first subset is made by MSs that were previously classified as such from low S/N and/or spectral resolution observations (Cotera et al. 1999; Muno et al. 2006; Mauerhan et al. 2007, 2010a,b; DeWitt et al. 2013; Dong et al. 2015; Geballe et al. 2019). These stars have the following characteristics: (i) have a Paschen α excess indicative of a powerful stellar wind (Dong et al. 2011), (ii) are associated with an X-ray source indicative of a colliding wind binary (Mauerhan et al. 2009), or (iii) their mid-IR properties are indicative of a highly luminous, potentially dust post-main-sequence star (Geballe et al. 2019). The second subset comprises the remaining candidates characterized by pronounced Paschen α emission from the catalogue of Dong et al. (2011), but they have not been spectroscopically classified yet. Other 17 MSs were returned from this cohort, with the remaining ∼30 stars comprising cool, low-mass interlopers along the LOS. In addition to these lists, we also considered MSs in the Arches cluster from Clark et al. (2018). We refer to the collection of MSs in our field not included in the Primary and Secondary lists of Paschen α emitters of Dong et al. (2011) simply as Other list.

The spectral-type characterization made by Clark et al. (in preparation) allow us to define three samples of objects: confirmed MSs, candidate MSs, and non-massive objects. In total, we measured the PM of 43 confirmed MSs, 64 candidate MSs, and 5 non-massive objects. The list of these objects is presented in Table D1. In the following, we discuss in detail the kinematics of the confirmed MSs, while we provide a shorter analysis for the candidate MSs and the non-MSs. Not all these objects, especially those at the faint end of our catalogues, passed all the astro-photometric quality selections described in Sections 2 and 3, but we study their kinematics anyway. In Table 2, we report positions and PMs of Sgr A* (from Reid & Brunthaler 2020), the Arches, and the Quintuplet (from Libralato et al. 2020) as a reference.

5.1 Confirmed MSs

5.1.1 Population structure and distribution

The location of confirmed MSs in the CMD (left-hand and middle-left panels of Fig. 14) suggests that almost all MSs have a Bulge/Bar origin, with only one possible interloper (green point). Blue and red points mark MSs in the blue and red side of the Bulge/Bar sequence in the CMD, respectively. This selection is not possible in the ACS/WFC field and we simply plot probable Bulge/Bar MSs redder than the arbitrarily colour $(m_{\rm F850LP} - m_{\rm F190N}) = 6.2$ as red points. The middle-right and right-hand panels of Fig. 14 present a comparison between the PMs of the MSs in the Primary, Secondary, and Other lists and the PMs of stars in the Disc (middle-right panels) and Bulge/Bar (right-hand panels) samples described in Section 4.1. We considered Disc and Bulge/Bar objects in the same magnitude interval of the MSs ($m_{\rm F190N} \lesssim 16$). The green point (star #18668 in the Primary list) has a PM similar to that of the Disc or Bulge/Bar stars. However, its position in different CMDs makes it challenging to infer its membership.

At a first glance, MSs have kinematic properties different from those of Disc stars within a few kpc from the Sun. The comparison between the PM distributions of the MSs and Bulge/Bar objects is not straightforward. Bulge/Bar objects along the LOS are located in a wide range of distances from Sgr A*, either in front or behind it, which reflect in different PM distributions along the $l\cos b$ direction. On the other hand, the PM distributions of Bulge/Bar objects at various distances from Sgr A* along the b direction in our VPD seem rather similar. We compared the μ_b PM distribution of MSs with those of Bulge/Bar objects. We selected only stars brighter than $m_{\rm F190N} = 13$ and with a PM error lower than 1 mas yr^{-1}, and measured their velocity dispersions σ_b. We find that Bulge/Bar stars have $\sigma_{\mu_b} = (2.06 \pm 0.02)$ mas yr^{-1}, while MSs have $\sigma_{\mu_b} = (0.95 \pm 0.17)$ mas yr^{-1}. The velocity dispersion of the MSs shown in blue in Fig. 14 is $\sigma_{\mu_b} = (0.79 \pm 0.17)$ mas yr^{-1}. These values suggest that most MSs are a distinct population from the rest of the Bulge/Bar stars chosen for the comparison. Specifically, their lower σ_{μ_b} (which corresponds to ∼30 km s^{-1} at the distance of the GC) indicates that they are a near-planar population that is not as vertically extended as the Galactic Bulge. The σ_{μ_b} of selected Bulge/Bar stars differs from what we would expect for stars very close to the GC (∼3 mas yr^{-1}). Because of the direction of the reddening vector and the magnitude cut at $m_{\rm F190N} = 13$, we are likely selecting objects in front of Sgr A* (see Section 4.1 and CMDs in Fig. 10) that have a different velocity dispersion than the Bulge population (e.g. Clarkson et al. 2008).

The MSs in blue in Fig. 14 seem part of a defined sequence in the CMD, and are clustered together in the VPD. Fig. 15 shows the $K_{\rm S}$ versus $(J - K_{\rm S})$ CMD for the stars in the WFC3/IR field (black points). Green points represent stars in the ACS/WFC field. As discussed in Section 4.2, stars in the ACS/WFC catalogue in common with the ancillary catalogues are Bulge/Bar objects closer to the Sun than those in the WFC3/IR catalogue. Again, blue points are the MSs in the blue side of the Bulge/Bar sequence. The colour width of these MSs in the CMD is similar to that of the Bulge/Bar stars shown in green with $(J - K_{\rm S}) \gtrsim 3.5$. This piece of evidence suggests that the MSs shown in blue in Fig. 14 could be in front of the GC, closer to the Sun than all other confirmed MSs, and could be part of the general 'field' population. Red points in Fig. 15 represent MSs that are likely members of the Arches from Clark et al. (2018). The similar CMD locations for these two groups of star could instead indicate that isolated and Arches' MSs are at the same distance. The different colours of MSs and Bulge/Bar objects shown in black in

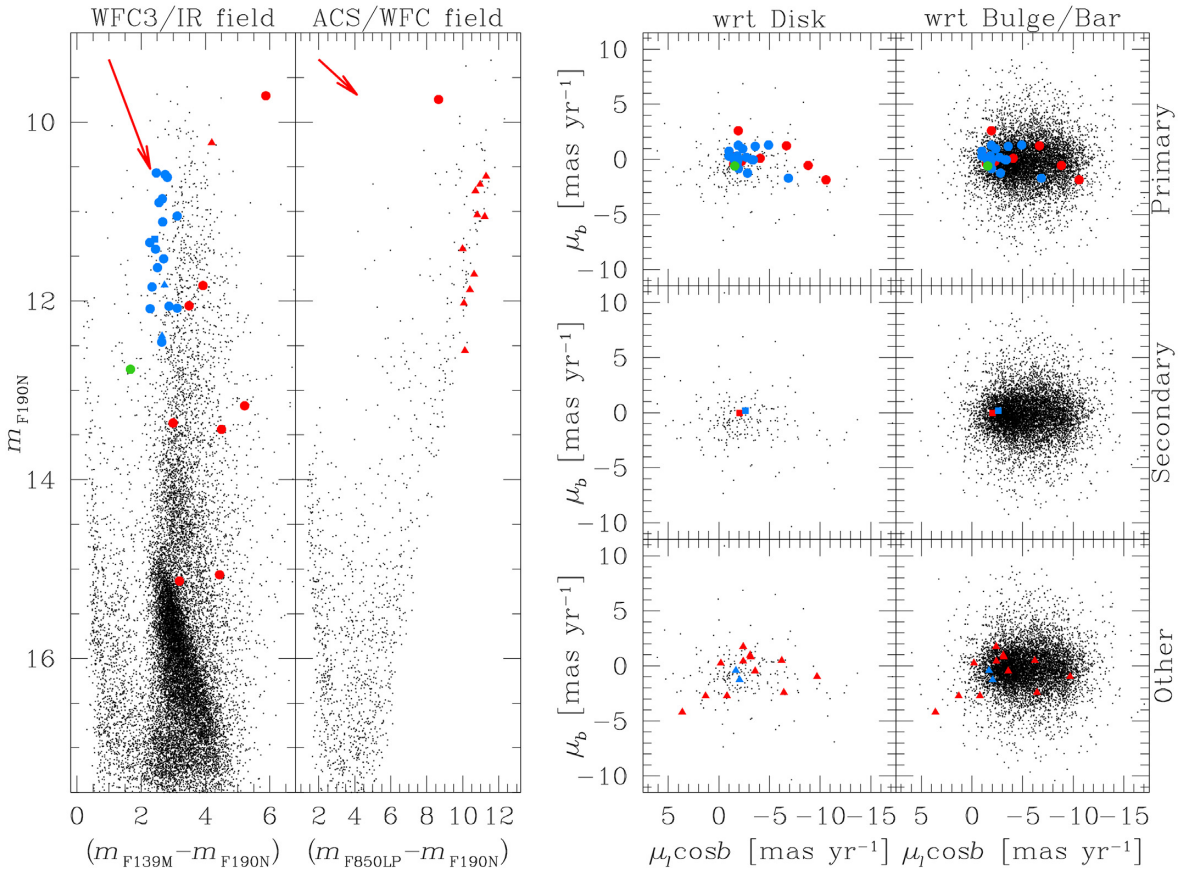

Figure 14. In the left-hand and middle-left panels, we plot the m_{F190N} versus $(m_{F139M} - m_{F190N})$ CMD for the stars in the WFC3/IR field and the m_{F850LP} versus $(m_{F850LP} - m_{F190N})$ CMD for the stars in the ACS/WFC field, respectively. We selected three samples of objects in the CMDs: Green points refer to stars bluer than the Bulge/Bar sequence, while blue (red) points are the bluest (reddest) MSs in the Bulge/Bar sequence. Circles, squares, and triangles represent confirmed MSs in the Primary, Secondary, and Other samples, respectively. The middle-right and right-hand panels show the VPDs of the PMs of the MSs in the Primary (top), Secondary (middle), and Other (bottom) lists compared to the samples of Disc and Bulge/Bar stars defined in Section 4.1, respectively.

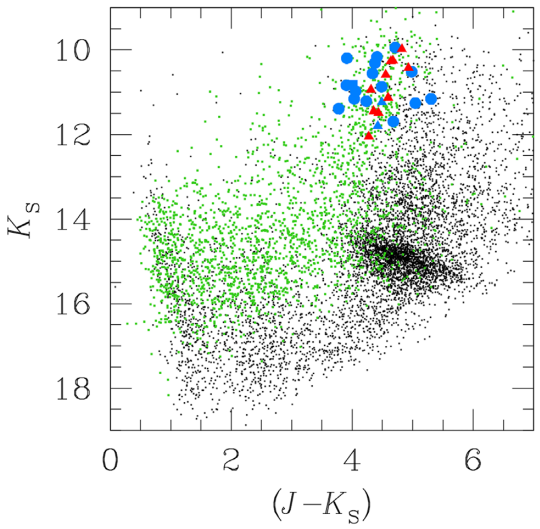

Figure 15. K_S versus $(J - K_S)$ CMD. Black points are stars in the WFC3/IR field, while green points represent stars in the ACS/WFC field. Blue points are the MSs in the blue side of the Bulge/Bar sequence as shown in Fig. 14. The MSs that are likely members of the Arches according to Clark et al. (2018) are shown as red triangles.

Fig. 15 could reflect the different intrinsic nature of the two groups of stars (young, massive objects versus old, low-mass stars). If the Arches is in the GC, isolated MSs shown in blue in Fig. 14 are in the GC as well, although they are not part of a cluster but general field objects. Finally, the relative position of Arches and Bulge/Bar stars in our CMD is qualitatively in agreement with those in the CMD shown in Hosek et al. (2019).

The MSs in our field could be born in star-forming regions in the Galaxy spiral arms and be just projected towards the GC, although it seems unlikely since they lie on the Bulge/Bar sequence on the CMDs. We investigated this hypothesis as follows. We simulated 1000 stars with the same Equatorial coordinates, equal to the average (R.A., Dec.) of the MSs in our field, but different distances from the Sun (0–10 kpc with steps of 0.01 kpc). The Galactocentric motion (V_X, V_Y, V_Z) of each object was assigned by means of the Galactic rotation curve measured by Reid et al. (2019). Specifically, we used their best model 'A5' and the code in their appendix B (rescaled by the distance of Sgr A* of 8.178 kpc of Gravity Collaboration 2019) to compute the circular rotation as a function of Galactocentric distance. We also simulated a peculiar motion for each source by introducing a velocity component along the radial direction from the GC (between −15 and 15 km s^{-1}). We decomposed these radial and circular velocities of each star in the (V_X, V_Y) velocities. V_Z was varied between −15 and 15 km s^{-1}, again to simulate a peculiar motion. Finally, we converted (V_X, V_Y, V_Z) into Galactic PMs and compared

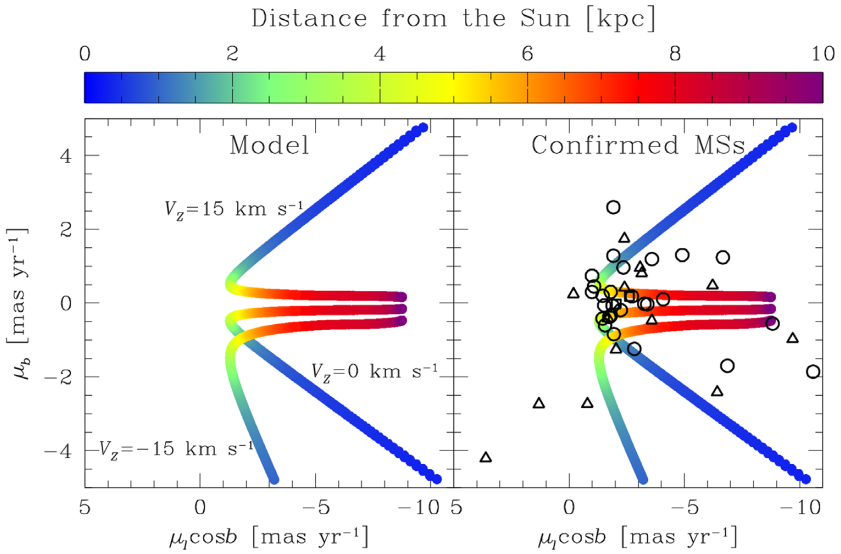

Figure 16. In each panel, we plot the VPDs of the Galactic PMs for a set of simulated Disc stars in the Galactic plane (see the text for details), colour coded according to the distance from the Sun. Black points in the right VPD show the PMs of the confirmed MSs. Open circles, squares, and triangles refer to objects in the Primary, Secondary, and Other lists, respectively.

them to the MS PMs. We neglected the influence of the Galactic Bar at small Galactocentric distances since we are mainly interested in the connection between MSs and the Galactic spiral arms. The result is shown in the left-hand panel of Fig. 16. Simulated points are colour coded according to their distance from the Sun (we plot only the extreme cases of radial Galactocentric motion of −15 and 15 km s^{-1} and $V_Z = -15$ or 15 km s^{-1} for clarity).

The comparison between the PMs of the confirmed MSs (right-hand panel) and our simulations shows that most MSs in the VPD have PMs that are not consistent with those of the Disc stars within 4 kpc from the Sun. If MSs are distant Disc stars and the discrepancy between observations and simulations is mainly due to unaccounted for peculiar motions or to the influence of the Bar, Fig. 16 seems to imply that most MSs are located in the innermost ∼3–4 kpc of the Galaxy. As stated in Reid et al. (2019), star-forming regions in the 3-kpc arm are likely associated with the Bar of the Galaxy rather than being a true spiral arm, while maser sources in the 4-kpc ('Norma') arm have large peculiar motion because they are near the end of the Bar. These pieces of evidence support a Bulge/Bar origin for most confirmed MSs. However, a distance of 3–4 kpc from the GC is unlikely for the following reasons. First, these stars are very bright and should have been visible in the *Gaia* catalogue if located at a distance of 3–4 kpc from the GC. Secondly, some isolated MSs have been associated with radio, X-ray, and/or mid-IR features known to be in the GC (e.g. Cotera et al. 1996). Finally, the extinction for these objects is larger than $A_V \gtrsim 20$ mag (Mauerhan et al. 2009), which would require an unusual, ad-hoc high extinction for spiral-arm objects at 3–4 kpc from Sgr A*. Therefore, the 3–4 kpc has to be considered an upper limit for the distance of MSs from Sgr A*.

Unfortunately, as we still lack distances, we cannot a priori discard origins within or outside the GC region. In the following, we assume these MSs to be close to the GC and investigate if any of them are associated with either Sgr A*, the Arches, or the Quintuplet.

If the confirmed MSs are in the GC region, the tight distribution in the VPD (Fig. 17) for most of them suggests that these MSs could have originated from the same molecular cloud orbiting around Sgr A*. The difference between the bulk PM of most MSs and the Arches and Quintuplet clusters is likely an indication that MSs and

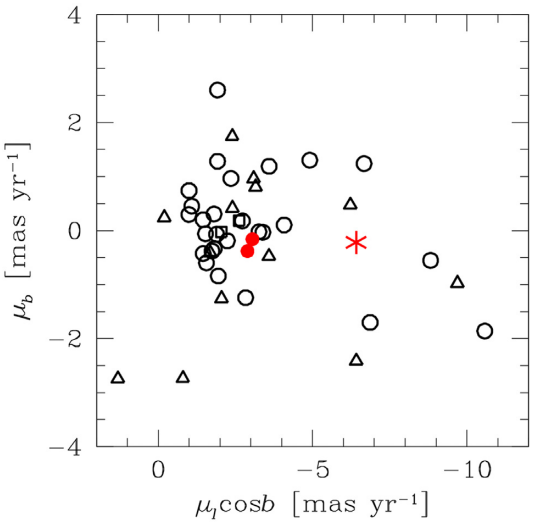

Figure 17. VPDs of the PMs of the confirmed MSs (black points). The red star marks the PM of Sgr A*, while the two red points indicate the PMs of the Arches and Quintuplet clusters. As in Fig. 14, circles, squares, and triangles represent MSs in the Primary, Secondary, and Other samples, respectively.

the clusters are experiencing a different Galactic potential and are at different distances from Sgr A*, with the MSs probably further from Sgr A* than the clusters. However, the PM difference between isolated MSs and the clusters could simply be due to different peculiar motions, and all these objects could be at the same distance from Sgr A*. Only a small group of objects have a broad PM distribution in the VPD and might represent the closest sample of MSs to the GC. A third component of the motion (LOS radial velocities) for the MSs is required to better constrain the location of their formation.

5.1.2 *Runaway star candidates*

Some MSs could indeed have been born in a cluster or close to Sgr A*, and then ejected. Even if we do not know the distance of

the MSs (nor those of the Arches and the Quintuplet), we can still select candidates whose PMs suggest that they are moving radially away from these possible birth places. First, we defined a reference system in which the possible origin source (Sgr A*, the Arches, or the Quintuplet) is at rest and at pixel (0, 0). Then, we computed the PM position angle θ between the direction of the PM vector and the direction of the star to the source. This angle is defined to be 0 deg if the star is moving radially from the source, and ±180 deg if it is moving radially towards the source. We defined as candidates all objects that verify the following conditions:

(i) $|\theta| < 10$ deg;

(ii) the closest distance to the origin backward in time, based on the relative PM vector ($\pm 1\sigma$), is equal or smaller than a limit radius. For Sgr A*, we defined the limit radius as its influence radius of ∼3 pc (Schödel et al. 2018), i.e. 1.26 arcmin at the distance of 8.178 kpc, while for the Arches and the Quintuplet, we used their angular size provided by the SIMBAD data base;[8]

(iii) the closest approach happened within the age of the origin source. For Sgr A*, we assumed an age of 6 Myr (as that of the Central Star Cluster; Martins et al. 2007). For the Arches and the Quintuplet, we considered ages of 2.5 Myr (Martins et al. 2008) and 4 Myr (Liermann et al. 2010), respectively.

We repeated the computation 1000 times, each time adding a random noise to the PM, and verified if conditions (i), (ii), and (iii) were met. The noise added to each star was randomly picked from a Gaussian distribution with σ equal to the PM error of the star. Stars measured in only one image per epoch do not have a PM error. For them, we assigned the median PM error of close-by stars at the same magnitude level. If a candidate passed all three conditions (i), (ii), and (iii) at least once, we inspected the results and discarded the candidate if its PM errors are too large (i.e. wide range of θ). An example of the results for the star #20612 is shown in Fig. 18.

In the reference system where Sgr A* is at rest and is placed at the origin of the coordinates, MSs escaped from the Sgr A* region are moving as the main stream of stars in the field (parallel to the Galactic plane, towards positive Galactic longitude l; see VPD in the inset in Fig. 18) and, according to Section 4.1, are likely in front of the GC. The Arches and Quintuplet clusters are located at the edge of the FoV and have eastward motions larger than most of the stars in the field. In the reference system where the Arches or the Quintuplet are at rest, most stars in our field are moving towards west and have a motion similar to what we expect for a star escaping from the clusters. These conditions (position and kinematics of the clusters) make the few MS escapers we found not that special, thus weakening the escaping nature of our potential MS escapers. Furthermore, the absolute PMs of MSs suggest that they might not be at the same distance of the clusters. All these features are probably an indication that these objects are not genuine escapers and their motion is just the result of perspective effect. The unknown distance of MSs is the limiting factor that prevents us from reaching definitive conclusions. Table 3 summarizes the parameters of these stars. We report the flight time of these objects, defined as the distance from the current position to the point of closest approach divided by the relative PM of the MS in the reference frame where the origin source (Sgr A*, the Arches, or the Quintuplet) is at rest. The quoted errors on the flight times are only internal and do not include any source of systematic errors.

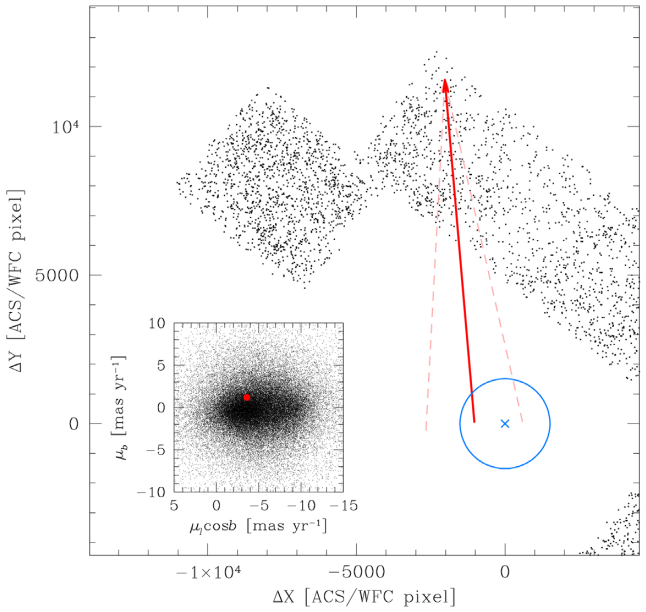

Figure 18. PM of the MS #20612 relative to Sgr A*. The red solid arrow starts at the time of the closest approach (see Table 3) and ends at the current position of the star. Pink dashed arrows define the confidence region. The blue circle has a radius of ∼1.26 arcmin and is centred on the position of Sgr A* (blue cross). The absolute PM of the source is shown in the VPD in the inset. Only 25 per cent of the bright sources are shown. North is up and east is to the left.

The MSs that appear to have come from Sgr A* are not HVSs, thus excluding the ejection via the Hill mechanism. Various mechanisms can eject stars over different time-scales. An ejection resulting from the disruption of a binary by a supernova explosion is plausible if the age of the star-forming region is longer than the shortest lifetime of a star (∼3 Myr; e.g. Zapartas et al. 2017). The ∼2.5-Myr age of the Arches disfavours supernova-related events for the candidate escapers. A three-body interaction can expel the least massive star in the system and leave behind a binary object made by two stars with a mass of at least 100 $M_\odot$ (the typical mass of the MSs in this sample; see Dong et al. 2015), larger than that of the ejected object. Mass segregation in the two clusters (e.g. Hosek et al. 2019; Rui et al. 2019) makes MSs to preferentially sink towards the cluster centre, favouring their dynamical interaction. Finding MS binary systems in the core of the Arches and the Quintuple would not contradict a three-body ejection mechanism as explanation for massive escapers. Nevertheless, the flight time of all these escapers is suspiciously small, thus suggesting a fortunate alignment of the PM vectors.

Star #1398622 in the ACS/WFC catalogue[9] in the Secondary list is classified as an ejected candidate from the Arches. Its absolute PM is in agreement with the bulk motion of the Arches within 1σ, suggesting that it could be a member of the cluster. The tidal radius of the Arches is about 1.6 pc (Habibi et al. 2013), which corresponds to ∼40 arcsec at the distance of Sgr A*. Even if the cluster is located 2 kpc in front of the GC (and its tidal radius becomes about 53 arcsec), star #1398622 would still be outside the tidal radius. For this reason, this star is an interesting target to follow up with LOS-radial-velocity measurements.

Fig. 19 presents the histograms (bin width of 10 deg) of the PM position angle θ of confirmed MSs with respect to Sgr A* (left-

[8]Wenger et al. (2000) and http://simbad.u-strasbg.fr/simbad/.

[9]Star #1398622 is measured in one image per epoch.

Table 3. Overview of the confirmed MSs selected as escaping candidates.

ID	ΔPM (mas yr^{-1})	θ (deg)	Flight time (Myr)	Possible origin	List	Spectral type
17180	4.89 ± 0.37	−8.6 ± 0.1	0.10 ± 0.01	Sgr A*	Primary	WC9
20255	4.73 ± 0.28	11.1 ± 0.1	0.11 ± 0.01	Sgr A*	Primary	B1-2 Ia+/WNLh
20612	3.15 ± 0.49	−4.7 ± 0.2	0.19 ± 0.01	Sgr A*	Primary	O6-7 Ia+
2061	6.71 ± 0.62	0.6 ± 0.1	0.22 ± 0.01	Arches	Other	WCLd
1398622	1.01 ± 0.69	2.0 ± 0.4	0.10 ± 0.04	Arches	Secondary	B1-3 Ia+
15593	4.19 ± 0.86	4.2 ± 0.3	0.08 ± 0.01	Quintuplet	Primary	O6-7 Ia+

Note. (i) The ΔPM in column (2) is relative to the origin source (i.e. the absolute PM of the origin source was subtracted from the PM of the star). (ii) The PM position angle θ and its error are defined as the median and the error to the median values, respectively, of the 1000 realizations of θ obtained as described in the text. (iii) WC = Carbon-type Wolf–Rayet; WN = Nitrogen-type Wolf–Rayet; O = O supergiant.

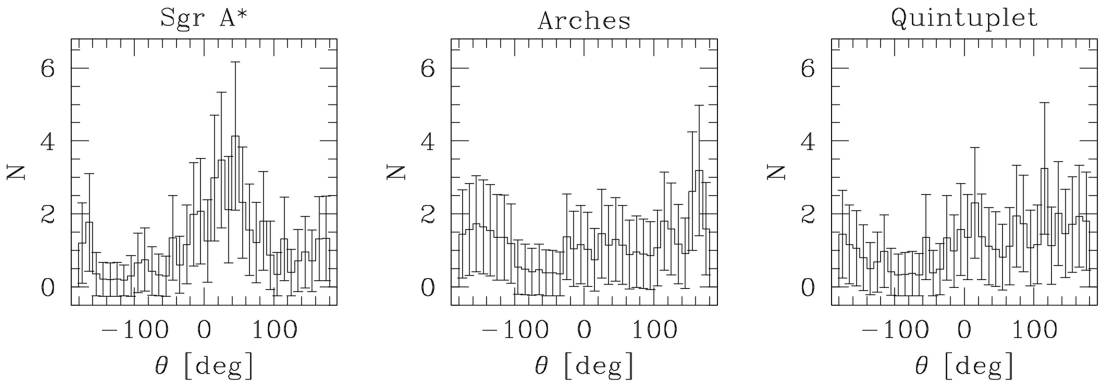

Figure 19. Histograms of the PM position angle θ for confirmed MSs. Error Bars are defined as $\sqrt{N}$. From left to right, we show the histograms of θ computed with respect to Sgr A*, the Arches, and the Quintuplet.

hand panel), the Arches (middle panel), or the Quintuplet (right-hand panel). Each histogram shown in the figure is the average of 1000 histograms, each of which was obtained by measuring θ after adding a random noise to the PM errors as described above. By adding the random noise, we randomly blurred/sharpened and shifted the distributions in the histograms. The final average histogram is less dependent on the bin width and the starting point (see e.g. Libralato et al. 2019). MSs do not show any significant peak at $\theta \sim 0$ deg in the histograms. There is a hint at the $\sim 2.8\sigma$ level of a peak at $\theta \sim 30$ deg in the histogram for Sgr A*. Given the relative position and PM of the confirmed MSs with respect to Sgr A*, we still favour the idea that the sample of potential escapers previously discovered is mainly the result of a perspective effect.

5.1.3 Arches' members

10 MSs in the ACS/WFC field close to the Arches are included in the list of Arches' MSs of Clark et al. (2018). The VPD of the PMs of these stars is shown in Fig. 20. The blue cross marks the PM of the Arches and the ellipse has semi-axes equal to the median PM errors of stars at the magnitude level of the 10 massive objects in that region of the FoV. Eight out of ten stars are likely members at the 1σ level, and all objects have PMs consistent with that of the Arches at the 2σ level. These MSs are listed in Table 4.

5.1.4 Cluster tidal tails

The confirmed MSs in our field could be former members of the Arches or the Quintuplet in a tidal tail of the clusters. Hosek et al.

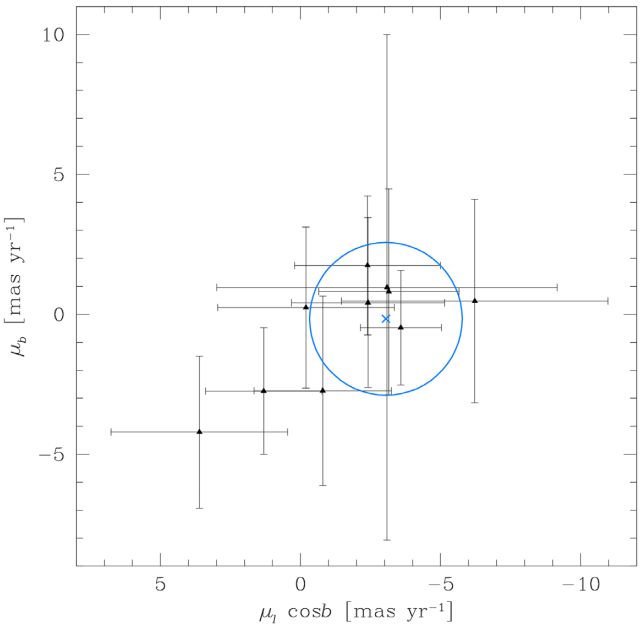

Figure 20. VPD of the absolute PMs of confirmed MSs in the ACS/WFC field close to the Arches (black triangles with error Bars). The blue cross marks the absolute PM of the Arches cluster. The blue ellipse is centred on the cross and has semi-axes equal to the median PM errors of stars at the magnitude level of the 10 massive objects.

Table 4. List of confirmed MSs' likely members of the Arches cluster.

ID	List	Spectral type
1412291	Other	WN8-9h
1412292	Other	WN8-9h
1412295	Other	WN8-9h
1412379	Other	O6-6.5 Ia
1412381	Other	O6-7 Ia+
1412382	Other	WN7-8h
1412383	Other	O4-5 Ia+
1412384	Other	WN8-9h
1412386	Other	O4-5 Ia
1412470	Other	WN8-9h

Note. (i) PMs of the stars #1412379, 1412383, 1412386, and 1412470 were measured with one image per epoch. (ii) All stars are included in the list of Arches' MSs of Clark et al. (2018).

(2019) and Rui et al. (2019) analysed in detail the Arches and Quintuplet clusters. Neither studies found hints of tidal-tail structures out to 3 pc from the clusters' centres, and the authors observed (weak for the Quintuplet and strong for the Arches) evidence of mass segregation. Both pieces of information make it unlikely to find MSs in a tidal tail. However, the GC region is very extreme, and a few massive objects could have been ejected at early stages of the clusters' evolution.

We defined the direction of motion of the clusters with respect to Sgr A* in the plane of the sky by means of the PMs listed in Table 2. Red and blue arrows in the left-hand panels in Fig. 21 represent the expected motion of the two clusters (the Arches on top and the Quintuplet on bottom, shown as green dots) over 10^5 yr backwards and forwards in time, respectively. Cyan and pink regions highlight the location of the leading and trailing tails given the PMs of the clusters relative to Sgr A* (we also took into account for the PM errors). Black points mark the locations of the confirmed MSs. MSs within the shaded regions are potential members of a tidal tail. The right-hand panels of Fig. 21 present the PMs of the MSs (only those within the cyan/pink regions further than three times the cluster's angular size from SIMBAD) relative to the Arches/Quintuplet as a function of the position relative to the cluster along the l direction. Any tidally lost star must have μ_b similar to that of the Arches or the Quintuplet. Red points are MSs that have μ_b within 1 mas yr^{-1} from that of the corresponding cluster, while black points are all other MSs. Stars in a leading/trailing tails should have a positive/negative PM relative to the cluster, respectively. Interestingly, position and motion of star #1398622 in our ACS/WFC catalogue are consistent with being part of the leading tail of the Arches. Again, all six kinematic parameters of the MSs and clusters are required to completely understand the location of their origin.

5.1.5 Candidate MSs

Fig. 22 shows the CMDs and the VPDs for the candidate MSs in our lists. Colour and shape codings are the same as in Section 5.1 and Fig. 14. Green points are likely interlopers in the disc. Five objects have a parallax measurement in the *Gaia* DR2, suggesting that they are located within 2 kpc from the Sun. The location of the remaining stars in CMDs based on different colour combinations indicates that the remaining stars are likely Disc objects as well. Therefore, we excluded all these 14 stars for which CMDs or the *Gaia*-DR2 parallaxes clearly rule out a Bulge/Bar connection. CMD locations and PMs of the remaining MS candidates suggest that these objects are likely in the Bulge/Bar.

Fig. 23 presents the K_S versus $(J - K_S)$ CMD of the stars in the WFC3/IR field. Stars highlighted in red are the candidate MSs likely located in the Bulge/Bar. Most MSs are in the Bulge red clump. We measured the velocity dispersion σ_b of these candidate MSs and, as a reference, of Bulge/Bar objects in the Bulge red clump. We find that candidate MSs have $\sigma_{\mu_b} = (2.18 \pm 0.41)$ mas yr^{-1}, while Bulge/Bar stars have a $\sigma_{\mu_b} = (2.88 \pm 0.01)$ mas yr^{-1}, thus suggesting that the two groups of objects could be at the same distance from Sgr A* at the $\sim 1.7\sigma$ level. These MS candidates are likely a more genuine Bulge/Bar 'field' population than the confirmed MSs discussed in Section 5.1.1.

In the left-hand panel of Fig. 24, we compare the absolute PMs of the candidate MSs with those of Sgr A* and the Arches and Quintuplet clusters. The right-hand panel of Fig. 24 shows a zoom-in around the location of most candidate MSs in the VPD. Blue circles represent the confirmed MSs analysed in Section 5.1. The PM distribution of candidate MSs is broader and less centred around the clusters' positions than that of the confirmed MSs, suggesting that stars in these two groups have a different origin. However, as for the confirmed MSs, we lack of LOS velocities and distances and we cannot exclude the possibility that they could have been born closer to the GC.

Similarly to the analyses described in Section 5.1.2, we computed the PM position angle θ for candidate MSs. We identified again a few potential escapers (Table 5) but their flight time is short (<0.6 Myr), as in the case of the confirmed MSs, and some objects passed all criteria for more than one origin. Fig. 25 presents the histogram of the PM position angle θ for candidate MSs. There is not a clear peak within $|\theta| < 10$ deg (escaping objects) in any histogram. Both the Arches and Quintuplet histograms present a significant ($>3\sigma$) peak at $\theta \sim 27$ and ~ 17 deg, respectively, but these peaks are likely due to the relative position and PM of the candidate MSs with respect to the clusters. All these pieces of evidence favour the idea that these potential escapers might in fact just be the result of perspective effects.

Finally, the majority of candidate MSs passed the tidal-tail test.

5.2 Non-MSs

Five stars in our lists have a spectral type that suggests that they cannot be classified as MSs. The m_{F190N} versus $(m_{F139M} - m_{F190N})$ CMD and the VPDs shown in Fig. 26 suggest these objects to be Bulge/Bar stars.

6 FAST-MOVING STARS

MSs represent the tip of the iceberg of the GC population of stars born around Sgr A* or in a cluster and later ejected as a result of dynamical effects. Some stars do not produce strong emission lines and cannot be detected in emission-line surveys, but we can still find some potential candidates thanks to PMs. It is unfeasible to search for all potential escapers among the myriad of stars in our FoV, but we can at least study objects with a relatively high PM.

We focused only on well-measured stars in the WFC3/IR field with a PM error lower than 2 mas yr^{-1}. Since we are interested in fast-moving objects, we also included in our sample stars that have a PM larger than 70 mas yr^{-1} (see the discussion in Section 3). We removed all stars that, according to their location in a CMD, are likely part of the foreground Disc population. We then analysed two samples of stars, one bright (stars brighter than $m_{F139M} \sim 18.8$, i.e.

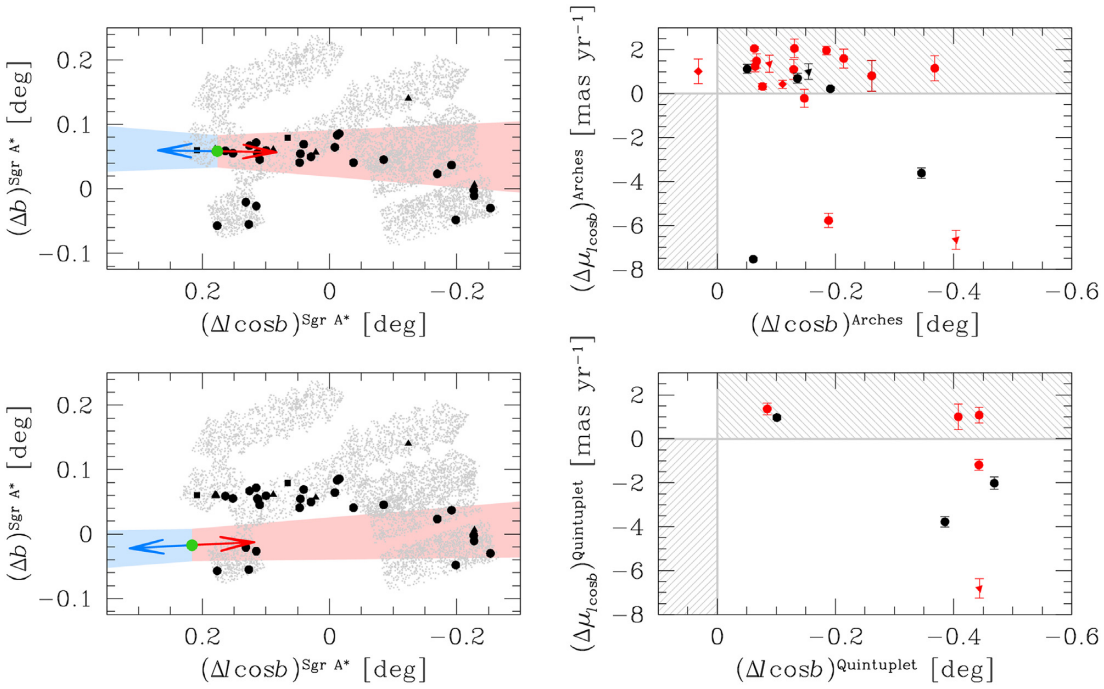

Figure 21. Top panels: in the left-hand panel, we show the FoV covered by our *HST* observations in the reference frame where Sgr A* is at rest. We highlighted in black confirmed MSs (circles, squares, and triangles represent MSs in the Primary, Secondary, and Other samples, respectively). The current Arches position is shown as a green point. All other bright stars are shown in grey. The future/past motion of the Arches in 10^5 yr is shown as a blue/red arrow. Cyan and pink regions mark the expected locations of the leading and trailing tails, respectively, of the cluster given the Arches' PM relative to Sgr A* (and its error). In the right-hand panel, we show the PM of the MSs relative to the Arches as a function of position relative to the Arches along the l direction. Only MSs within the cyan or pink regions outside three times the cluster's angular size (from SIMBAD) are considered. Stars in the grey areas are likely not part of the tidal tail (see the text for details). Red points are MSs that have $|\Delta\mu_b^{\rm Arches}| \leq 1$ mas yr^{-1}. All other points are shown in black. Bottom panels: as above, but for the Quintuplet cluster.

with a magnitude similar to that of the confirmed MSs) and one faint (all other objects). This choice is motivated by the fact that bright and faint stars have different PM errors and the interpretation of the results requires different considerations.

For each star, we computed its relative PM with respect to Sgr A*, the Arches, or the Quintuplet. Stars in the GC have a velocity dispersion of more than 100 km s^{-1}, which corresponds to about 3 mas yr^{-1} at the distance of Sgr A*. Therefore, we kept only sources with a PM larger than 10 mas yr^{-1}, i.e. three times the typical velocity dispersion in the GC. Finally, we measured their PM position angles θ.

Fig. 27 presents the results. In the left-hand panels, we show the histograms of the relative PMs with respect to the Quintuplet (top panels), the Arches (middle panel), and Sgr A* (bottom panel). The bright sample is in blue, while the faint sample is shown in red. Both groups have similar histograms. The histograms of the PM position angle θ of fast-moving objects are displayed in the right-hand panels.

The shape of the histograms of the PM position angles shown in Fig. 27 can be again explained by the peculiar location of Sgr A*, the Arches, and the Quintuplet in our field. Stars are located all around (both north and south, east and west, of) Sgr A*, in front or behind it. As such, the distribution of θ is expected to be flat.

The histograms of the bright stars in the two massive clusters show hints of a peak at $\theta \sim 0$ deg, with a sharp drop out around $\pm$90 deg. This can be explained in terms of selection effects: The PM distribution of Bulge/Bar stars is broader along the $l\cos b$ direction than the b direction, so that any selection based solely on PM size disproportionately favours stars with larger $\mu_l \cos b$. Faint stars, on the other hand, are able to populate all position angles: This is most likely due to the fact that their much larger PM errors make the PM distribution broader, and stars moving mainly along the b direction can still survive the selection based on PM size. For this reason, the histograms of the faint stars show rather flat distributions. The peak at $\theta \sim 0$ deg can be interpreted as discussed in Section 5.

If we restrict our analysis to stars with a PM larger than 26 mas yr^{-1} ($\sim$1000 km s^{-1} at 8.178 kpc), we find three stars in the WFC3/IR region escaping from Sgr A* ($|\Delta\theta| \lesssim 10$ deg). A visual inspection of the WFC3/IR stacked images reveals the presence of additional very faint, fast-moving objects not detected by our reduction software. However, the WFC3/IR cosmetic and angular resolutions are worse than that of ACS/WFC and, with only two epochs of data, it is not straightforward to infer if they are genuine HVSs or image artefacts. Among bright stars, in which PM measurements are more robust, we do not find any HVS candidate.

Brown (2015) estimates that, assuming a continuous and isotropic ejection of HVSs, the density of HVSs should scale as r^{-2} kpc^{-3}, with r the distance from Sgr A*. Our observations cover part of an annulus in the plane of the sky centred on Sgr A* with inner and outer radii of 3 ($\sim$7 pc at 8.178 kpc) and 17 arcmin ($\sim$40 pc), respectively. According to the relation of Brown (2015), we should expect $\sim$1 HVS within a spherical region of radius 40 pc around Sgr A*. However, we are not mapping the entire volume of this sphere centred on Sgr A* but only part of a spherical shell, and HVSs could not be ejected continuously and isotropically. For these reasons, the number of HVSs we should find in our field is likely less than 1. If we focus on bright stars, our null-detection would be in agreement

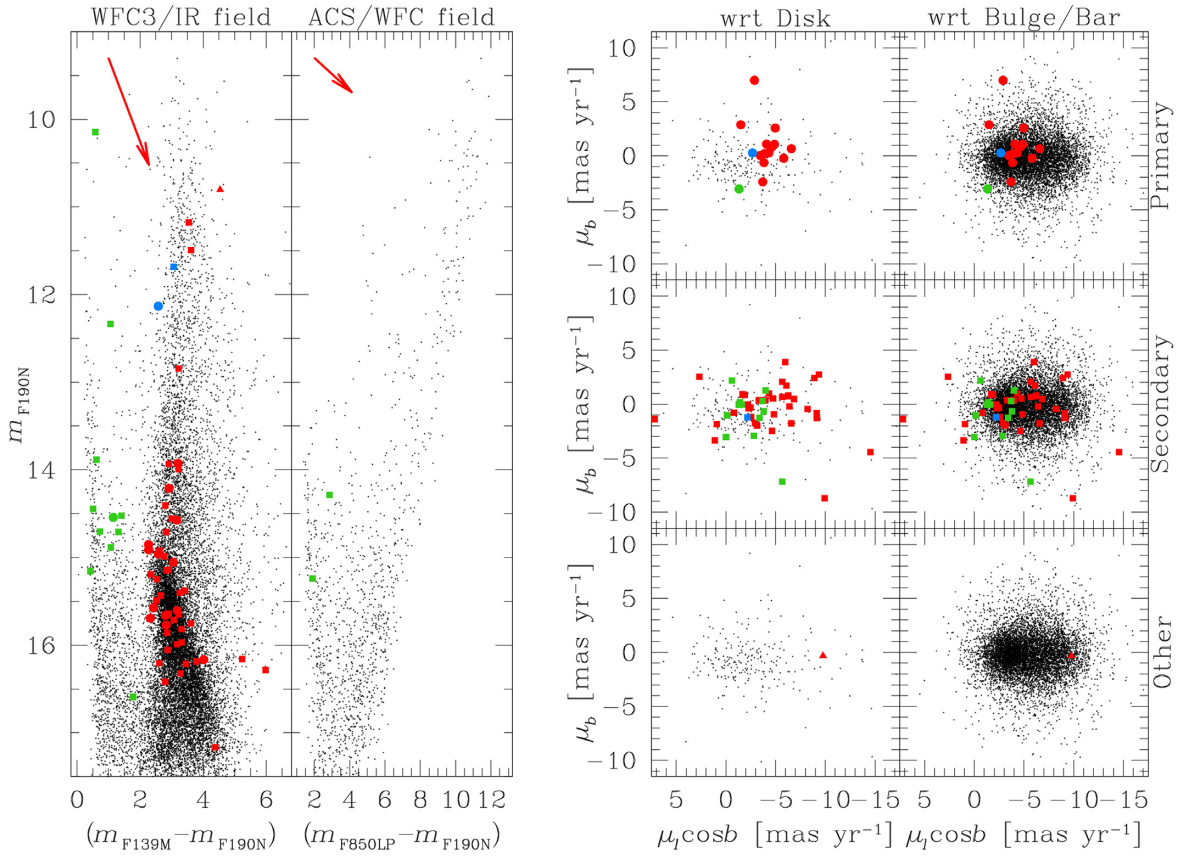

Figure 22. Similar to Fig. 14 but for candidate MSs.

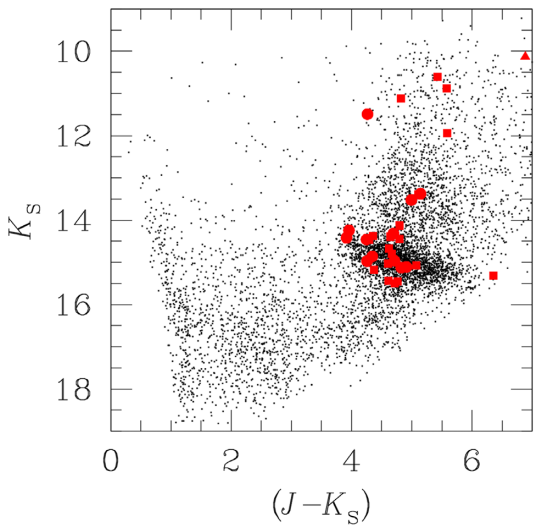

Figure 23. K_S versus $(J - K_S)$ CMD for stars in the WFC3/IR field (black points). Candidate MSs are shown as red points.

with the theoretical expectations. However, this result is biased by the small region analysed in our work and the lack of LOS data (we cannot detect HVSs with a motion predominantly along the LOS and not in the plane of the sky). A larger FoV and complementary LOS-velocity data are needed to reach a definitive conclusion about HVSs in the GC.

We do not find significant fast-moving Bulge/Bar stars in the ACS/WFC field.

7 CONCLUSIONS

The location of the origin of MSs in the GC region is still a matter of debate. Many pieces of information have been collected to investigate the nature of these massive objects, but we still need some key elements to fully reconstruct their history. In an effort to further shed light on these MSs, we computed high-precision PMs of stars near the GC with the *HST* data, and analysed the kinematics of confirmed and candidate MSs in the field. We make our astro-photometric catalogues publicly available. The description of the catalogues is provided in Appendix C. The lack of LOS velocities and distances of our targets is now the main source of uncertainty of our work and makes some of the conclusions mainly speculations. However, PMs allow us to provide constraints for some proposed scenarios even without a complete analysis of the Bulge kinematics.

The location of the origin of most confirmed, isolated MSs is still uncertain. We estimate an upper limit for their distance from Sgr A* of 3–4 kpc by comparing the PMs of the MSs with those of spiral-arm objects. Photometric and kinematic properties of these isolated MSs are different from what we would expect for a genuine population in the GC. However, their nature (young, MSs), the high and variable extinction, and peculiar motions (like those of the Arches and the Quintuplet) could explain the discrepancies we observe in CMDs and VPDs. As such, most of these isolated MSs could be in the GC, born a few Myr ago *in situ* from a single molecular cloud. A few objects might be former members of the Central Cluster, the Arches,

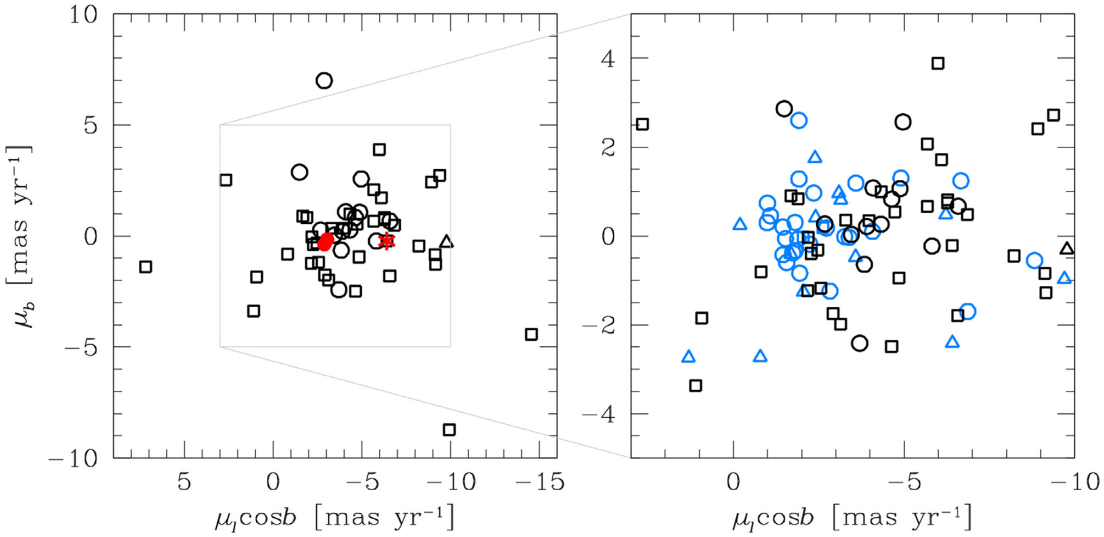

Figure 24. VPDs of the candidate MSs (black points). The red asterisk marks the PM of Sgr A*, while the two red points indicate the PMs of the Arches and Quintuplet clusters. As in Fig. 14, circles, squares, and triangles represent MSs in the Primary, Secondary, and Other samples, respectively. The right-hand panel is a zoomed-in view of the left-hand panel, in which we also plot in blue the confirmed MSs in our field, as a reference.

Table 5. Overview of the candidate MSs selected as likely escapers.

ID	ΔPM (mas yr^{-1})	θ (deg)	Flight time (Myr)	Possible origin	List
427662	1.83 ± 1.08	−4.8 ± 0.9	0.25 ± 0.08	Sgr A*	Secondary
1101618	4.13 ± 0.83	−10.4 ± 0.3	0.12 ± 0.02	Sgr A*	Secondary
1187124	0.59 ± 0.78	−5.1 ± 1.6	0.62 ± 0.28	Sgr A*	Primary
1210224	2.97 ± 0.81	−4.0 ± 0.3	0.16 ± 0.03	Sgr A*	Primary
1274214	7.52 ± 1.13	7.0 ± 0.2	0.07 ± 0.01	Sgr A*	Secondary
12280	6.73 ± 0.72	3.8 ± 0.1	0.13 ± 0.01	Arches	Other
236988	6.22 ± 0.34	2.5 ± 0.1	0.21 ± 0.01	Arches	Secondary
427662	5.19 ± 1.08	9.3 ± 0.3	0.24 ± 0.02	Arches	Secondary
656883	3.36 ± 0.88	−0.9 ± 0.3	0.34 ± 0.05	Arches	Secondary
1117192	3.38 ± 1.06	0.3 ± 0.4	0.12 ± 0.03	Arches	Secondary
1354402	1.60 ± 0.79	−3.9 ± 0.4	0.18 ± 0.04	Arches	Secondary
427662	5.34 ± 1.08	−2.0 ± 0.3	0.24 ± 0.03	Quintuplet	Secondary
1026874	6.26 ± 1.10	7.7 ± 0.3	0.06 ± 0.01	Quintuplet	Secondary
1187124	2.93 ± 0.78	6.4 ± 0.4	0.10 ± 0.01	Quintuplet	Primary

Note. (i) Star #427662 passed the criteria for Sgr A*, the Arches, and the Quintuplet. Star #1187124 passed the criteria for both Sgr A* and the Quintuplet.

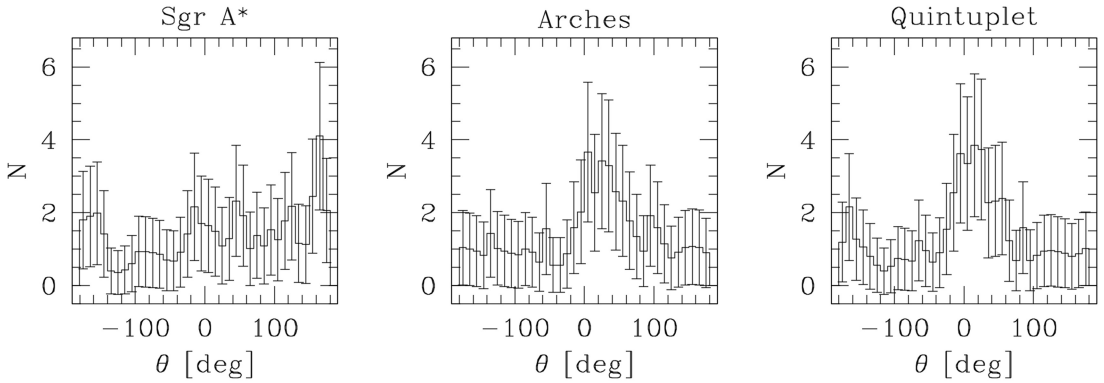

Figure 25. The histograms of the PM position angle θ for the candidates MSs (error Bars are defined as $\sqrt{N}$). The histograms for θ computed with respect to Sgr A*, the Arches, and the Quintuplet are show in the left-hand, middle, and right-hand panels, respectively.

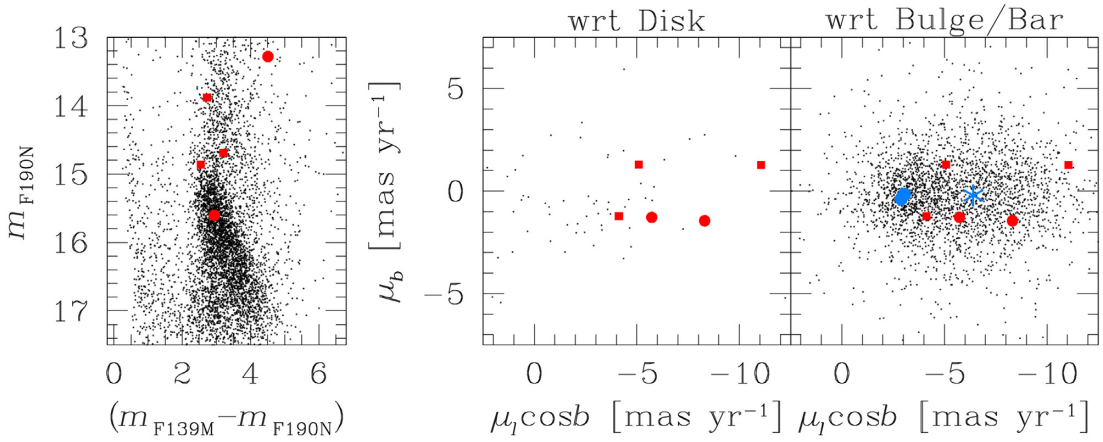

Figure 26. Left-hand panel: m_{F190N} versus $(m_{F139M} - m_{F190N})$ CMD for the stars in the WFC3/IR field. Red points represent the non-massive objects found in our list; all other stars are shown in black. Middle and right-hand panels: VPDs of the PMs for a sample of Disc (middle panel) and Bulge/Bar (right-hand panel) stars (black points). Red points have the same meaning as in the CMD. Blue dots show the absolute PMs of the Arches and the Quintuplet, while the blue star indicates the motion of Sgr A*.

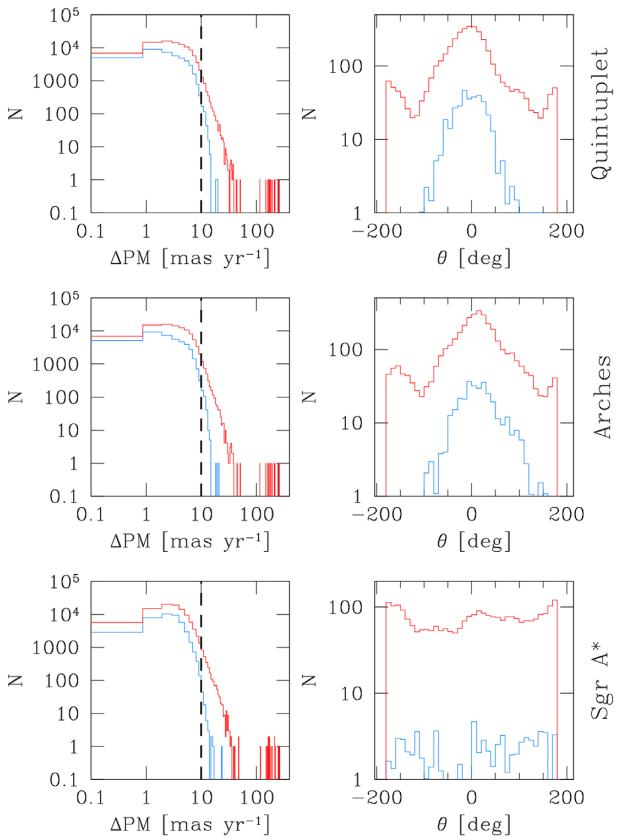

Figure 27. The histograms of the relative PMs with respect to the Quintuplet (top), the Arches (middle), and Sgr A* (bottom) are shown in the left-hand panels. Blue and red contours represent the histograms for stars brighter and fainter than $m_{F139M} \sim 18.8$, respectively. The black, dashed vertical lines sets the threshold for the selection of fast-moving objects. In the right-hand panels, we show the histograms of the PM position angle θ for the fast-moving stars.

or the Quintuplet, either ejected at velocities lower than 1000 km s^{-1} or part of a tidal-tail structure. Thanks to our PMs, we add strength to the argument that a selection of previously classified MSs are in fact likely Arches' members (in agreement with Clark et al. 2018). One object (star #1398622 in our ACS/WFC catalogue) in the Secondary list of Dong et al. (2011) is one of the most interesting targets because it is located outside the nominal tidal radius of the Arches and its kinematics is consistent with being an Arches' (former) member.

We also analysed a sample of MSs that still require a clear spectroscopic characterization. We excluded Disc interlopers from our list by means of *Gaia*-DR2 parallaxes, optical–NIR CMDs, and PMs. Most of the remaining candidate MSs are consistent with a Bulge/Bar field population according to their locations in CMDs and VPDs. The PM position angles of candidate MSs support an *in-situ* formation.

We searched our data set for fast-moving objects that could have been radially ejected from Sgr A*, the Arches, or the Quintuplet. The histograms of the PM position angles show no clear excess of high-velocity escapers. The peaks in these histograms can be simply interpreted by taking into account for the location of our FoV with respect to Sgr A* or the clusters, and the overall kinematics of the stars towards the GC. Large FoVs and LOS-velocity data are needed to complete the census of fast-moving objects in the GC.

Additional follow-ups to obtain LOS velocities are required to give a full 3D kinematic picture of this region. Furthermore, an additional third epoch of data, possibly with the *James Webb Space Telescope*, would further improve the astrometric precision and overall quality of our catalogues, and would allow us to further explore the wealth of information in this GC region.

ACKNOWLEDGEMENTS

ML and AB acknowledge support from STScI grants GO 12915 and 13771. DJL acknowledges support from the Spanish Government Ministerio de Ciencia, Innovación y Universidades through grants PGC-2018-091 3741-B-C22 and from the Canarian Agency for Research, Innovation and Information Society (ACIISI), of the Canary Islands Government, and the European Regional Development Fund (ERDF), under grant with reference ProID2017010115. LRP acknowledges support from the Generalitat Valenciana through the grant PROMETEO/2019/041. LRB acknowledges partial support by MIUR under PRIN programme no. 2017Z2HSMF. The authors thank the anonymous referee for the useful comments and suggestions. This work has made use of data from the European Space Agency (ESA) mission *Gaia* (https://www.cosmos.esa.int/gaia), processed

by the *Gaia* Data Processing and Analysis Consortium (DPAC; https://www.cosmos.esa.int/web/gaia/dpac/consortium). Funding for the DPAC has been provided by national institutions, in particular the institutions participating in the *Gaia* Multilateral Agreement. This research made use of Astropy,[10] a community-developed core PYTHON package for Astronomy (Astropy Collaboration 2013, 2018). This research has made use of the SIMBAD data base, operated at CDS, Strasbourg, France.

DATA AVAILABILITY

The catalogues described in this article are available in the article and its online supplementary material.

REFERENCES

Anderson J., 2016, Instrument Science Report WFC3 2016-12, Empirical Models for the WFC3/IR PSF. STScI, Baltimore, MD, USA
Anderson J., Bedin L. R., 2010, PASP, 122, 1035
Anderson J., King I. R., 2006, Instrument Science Report ACS 2006-01. p. 34
Anderson J., van der Marel R. P., 2010, ApJ, 710, 1032
Astropy Collaboration, 2013, A&A, 558, A33
Astropy Collaboration, 2018, AJ, 156, 123
Bedin L. R., Fontanive C., 2018, MNRAS, 481, 5339
Bedin L. R., King I. R., Anderson J., Piotto G., Salaris M., Cassisi S., Serenelli A., 2008, ApJ, 678, 1279
Bellini A. et al., 2014, ApJ, 797, 115
Bellini A., Anderson J., Bedin L. R., King I. R., van der Marel R. P., Piotto G., Cool A., 2017a, ApJ, 842, 6
Bellini A., Anderson J., van der Marel R. P., King I. R., Piotto G., Bedin L. R., 2017b, ApJ, 842, 7
Bellini A. et al., 2018, ApJ, 853, 86
Bressan A., Marigo P., Girardi L., Salasnich B., Dal Cero C., Rubele S., Nanni A., 2012, MNRAS, 427, 127
Brown W. R., 2015, ARA&A, 53, 15
Clark J. S., Lohr M. E., Najarro F., Dong H., Martins F., 2018, A&A, 617, A65
Clarkson W. et al., 2008, ApJ, 684, 1110
Cotera A. S., Erickson E. F., Colgan S. W. J., Simpson J. P., Allen D. A., Burton M. G., 1996, ApJ, 461, 750
Cotera A. S., Simpson J. P., Erickson E. F., Colgan S. W. J., Burton M. G., Allen D. A., 1999, ApJ, 510, 747
de Mink S. E., Sana H., Langer N., Izzard R. G., Schneider F. R. N., 2014, ApJ, 782, 7
DeWitt C., Bandyopadhyay R. M., Eikenberry S. S., Sellgren K., Blum R., Olsen K., Bauer F. E., Sarajedini A., 2013, AJ, 146, 109
Dong H. et al., 2011, MNRAS, 417, 114
Dong H., Mauerhan J., Morris M. R., Wang Q. D., Cotera A., 2015, MNRAS, 446, 842
Gaia Collaboration, 2016, A&A, 595, A1
Gaia Collaboration, 2018a, A&A, 616, A1
Gaia Collaboration, 2018b, A&A, 616, A12
Geballe T. R., Lambrides E., Schlegelmilch B., Yeh S. C. C., Goto M., Westrick C., Oka T., Najarro F., 2019, ApJ, 872, 103
Genzel R., Eisenhauer F., Gillessen S., 2010, Rev. Mod. Phys., 82, 3121
Gravity Collaboration, 2019, A&A, 625, L10
Habibi M., Stolte A., Brandner W., Hußmann B., Motohara K., 2013, A&A, 556, A26
Habibi M., Stolte A., Harfst S., 2014, A&A, 566, A6
Hills J. G., 1988, Nature, 331, 687
Hosek M. W., Jr, Lu J. R., Anderson J., Najarro F., Ghez A. M., Morris M. R., Clarkson W. I., Albers S. M, 2019, ApJ, 870, 44
Lamb J. B., Oey M. S., Werk J. K., Ingleby L. D., 2010, ApJ, 725, 1886
Libralato M. et al., 2018b, ApJ, 861, 99
Libralato M. et al., 2019, ApJ, 873, 109
Libralato M., Fardal M., Lennon D., van der Marel R. P., Bellini A., 2020, MNRAS, 497, 4733
Liermann A., Hamann W.-R., Oskinova L. M., Todt H., Butler K., 2010, A&A, 524, A82
Lindegren L. et al., 2018, A&A, 616, A2
Martins F. et al., 2007, A&A, 468, 233
Martins F., Hillier D. J., Paumard T., Eisenhauer F., Ott T., Genzel R., 2008, A&A, 478, 219
Mauerhan J. C., Muno M. P., Morris M., 2007, ApJ, 662, 574
Mauerhan J. C., Muno M. P., Morris M. R., Bauer F. E., Nishiyama S., Nagata T., 2009, ApJ, 703, 30
Mauerhan J. C., Cotera A., Dong H., Morris M. R., Wang Q. D., Stolovy S. R., Lang C., 2010a, ApJ, 725, 188
Mauerhan J. C., Muno M. P., Morris M. R., Stolovy S. R., Cotera A., 2010b, ApJ, 710, 706
Muno M. P., Bower G. C., Burgasser A. J., Baganoff F. K., Morris M. R., Brandt W. N., 2006, ApJ, 638, 183
Nardiello D. et al., 2018, MNRAS, 481, 3382
Nogueras-Lara F. et al., 2018, A&A, 620, A83
Nogueras-Lara F. et al., 2019, A&A, 631, A20
Oey M. S., King N. L., Parker J. W., Watson A. M., Kern K. M., 2004, RMxAC, 22, 127
Parker R. J., Goodwin S. P., 2007, MNRAS, 380, 1271
Plazas A. A., Shapiro C., Smith R., Huff E., Rhodes J., 2018, PASP, 130, 065004
Reid M. J., Brunthaler A., 2020, ApJ, 892, 39
Reid M. J. et al., 2019, ApJ, 885, 131
Renzo M. et al., 2019, A&A, 624, A66
Rich R. M., Ryde N., Thorsbro B., Fritz T. K., Schultheis M., Origlia L., Jönsson H., 2017, AJ, 154, 239
Rui N. Z., Hosek M. W., Lu J. R., Clarkson W. I., Anderson J., Morris M. R., Ghez A. M., 2019, ApJ, 877, 37
Sabbi E. et al., 2016, ApJS, 222, 11
Schödel R., Gallego-Cano E., Dong H., Nogueras-Lara F., Gallego-Calvente A. T., Amaro-Seoane P., Baumgardt H., 2018, A&A, 609, A27
Stolte A. et al., 2015, A&A, 578, A4
Surot F. et al., 2019, A&A, 629, A1
Wang Q. D. et al., 2010, MNRAS, 402, 895
Wenger M. et al., 2000, A&AS, 143, 9
Zapartas E. et al., 2017, A&A, 601, A29

SUPPORTING INFORMATION

Supplementary data are available at *MNRAS* online.

Table C1. First 10 lines of the WFC3/IR F139M photometric catalogue based on the GO-12915 data.
Table C3. First 10 lines of the WFC3/IR PM catalogue.
Table D1. First 10 lines of the list of confirmed MSs, candidate MSs, and non-massive objects analysed in Section 5.

Please note: Oxford University Press is not responsible for the content or functionality of any supporting materials supplied by the authors. Any queries (other than missing material) should be directed to the corresponding author for the article.

APPENDIX A: COMPARISON WITH *GAIA*-DR2 PMS

Fig. A1 shows a comparison between the *HST*-based and *Gaia*-DR2 PMs. The red lines are the plane bisectors, the blue lines (not always visible) are the weighted straight-line fits to the points. Stars in common between *HST* and *Gaia* are bright Disc objects. These plots

[10] http://www.astropy.org

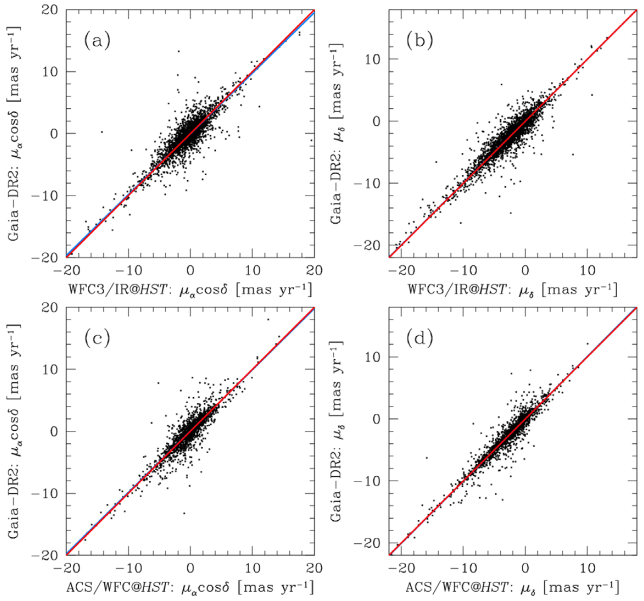

Figure A1. Comparison between *Gaia*-DR2 PMs and WFC3/IR (panels a and b) or the ACS/WFC (panels c and d) PMs. In each panel, the red line is the plane bisector, while the blue lines (when not hidden below the red lines) represent the weighted straight-line fit to the points.

show that there is good agreement between the two sets of PMs. Fig. A2 compares the PM errors of stars in common between the *Gaia* DR2 and our *HST* catalogues. At the faint-end of *Gaia* ($G \gtrsim 18$), our *HST* PM errors are a factor of 2 smaller than in the *Gaia* catalogue.

Fig. A3 presents a comparison between *Gaia* DR2 and *HST* PMs as a function of the *X* and *Y* positions in the FoV. The largest deviations (all within 3σ) are visible at the edges of the FoV. In these regions, the local network of reference stars used to transform *HST* positions on to the master frame is not uniformly distributed, thus possibly introducing some systematic error that can propagate to PM measurements.

The comparisons between the WFC3/IR-based and *Gaia*-DR2 PMs as a function of the $(G - m_{\rm F139M})$ colour and $m_{\rm F139M}$ magnitude are shown in the left-hand panels of Fig. A4. Similar comparisons between ACS/WFC and *Gaia* PMs as a function of $(G - m_{\rm F850LP})$ and $m_{\rm F850LP}$ are shown in the right-hand panels. Again, our PMs are in agreement with those of *Gaia* at the 3σ level. A systematic trend

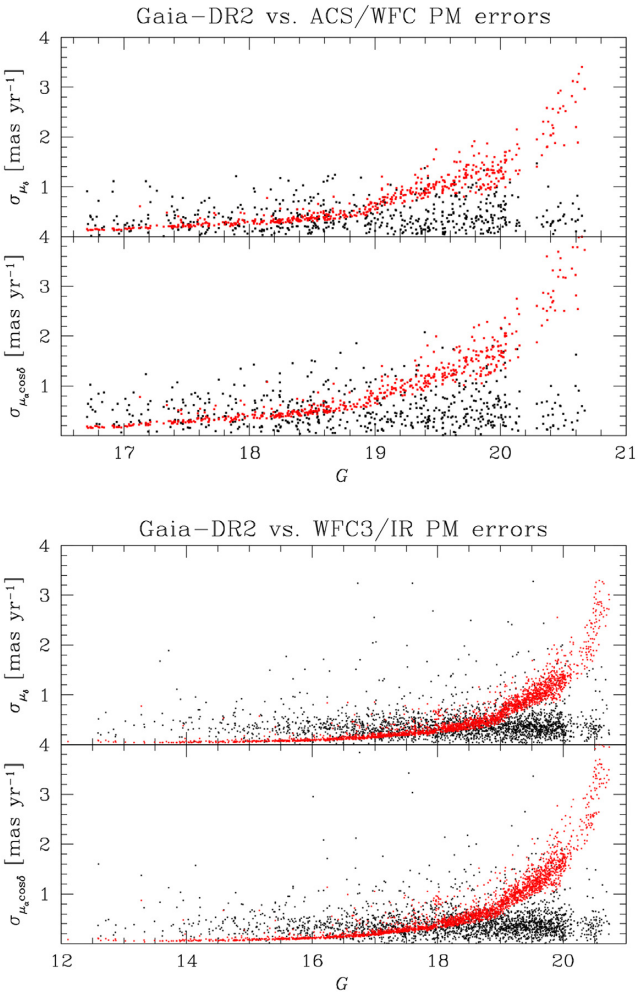

Figure A2. PM errors in the *Gaia* DR2 (red points) and our *HST* catalogues (black points) as a function of the *G* magnitude. ACS/WFC PM errors are in the top panels, while WFC3/IR PM errors are in the bottom panels.

as a function of colour for stars redder than the bulk of the Disc sequence is present. However, most stars in this colour range have $G > 18.5$ (see CMDs in Fig. A5); i.e. their *Gaia* PM errors are large. *Gaia* PMs in this faint regime are not generally used in our kinematic analyses.

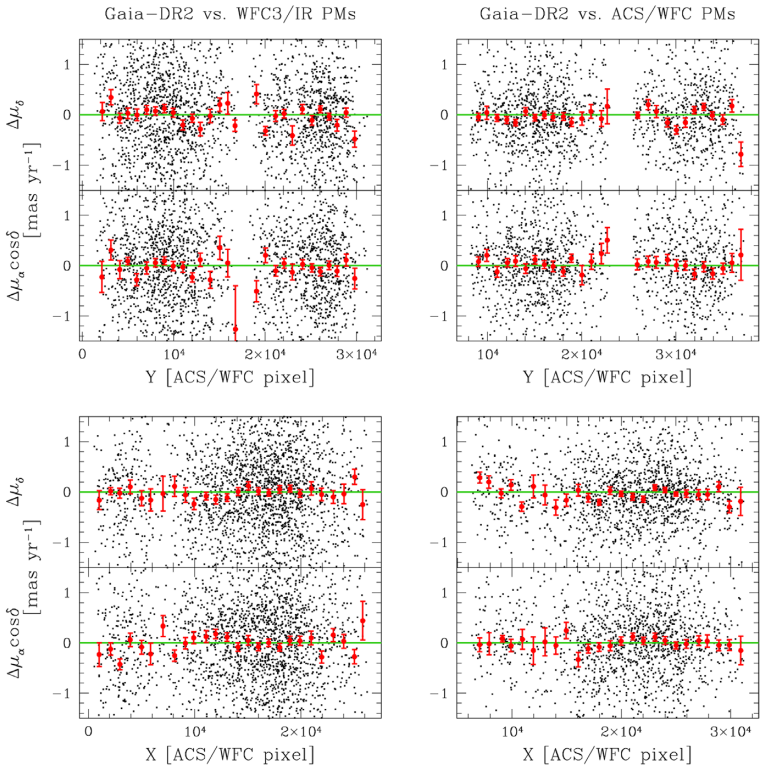

Figure A3. PM difference between *Gaia* and WFC3/IR (left) or ACS/WFC (right) PMs as a function of the *Y* (top panels) and *X* (bottom panels) positions in the FoV. Black points are all stars in common, and red dots (with error Bars) are the median values of the PM difference over 1000-pixel-wide bins. The green line is set at 0 mas yr^{-1}.

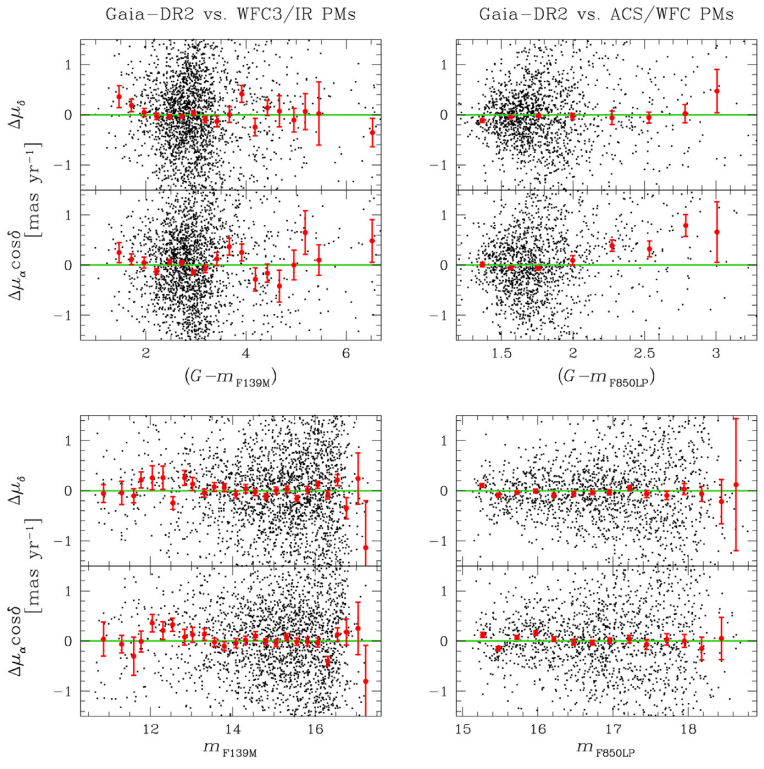

Figure A4. Left-hand panels: PM difference between *Gaia* and WFC3/IR PMs as a function of $(G - m_{\rm F139M})$ (top panels) and $m_{\rm F139M}$ (bottom panels). As in Fig. A3, the green line is set at 0 mas yr^{-1}. Black points represent individual stars, and red points (with error Bars) are the median values of the PM differences over 0.25-mag-wide bins. Right-hand panels: PM difference between *Gaia* and ACS/WFC PMs as a function of $(G - m_{\rm F850LP})$ (top panels) and $m_{\rm F850LP}$ (bottom panels). Colour coding and bin sizes are the same as in the left-hand panels.

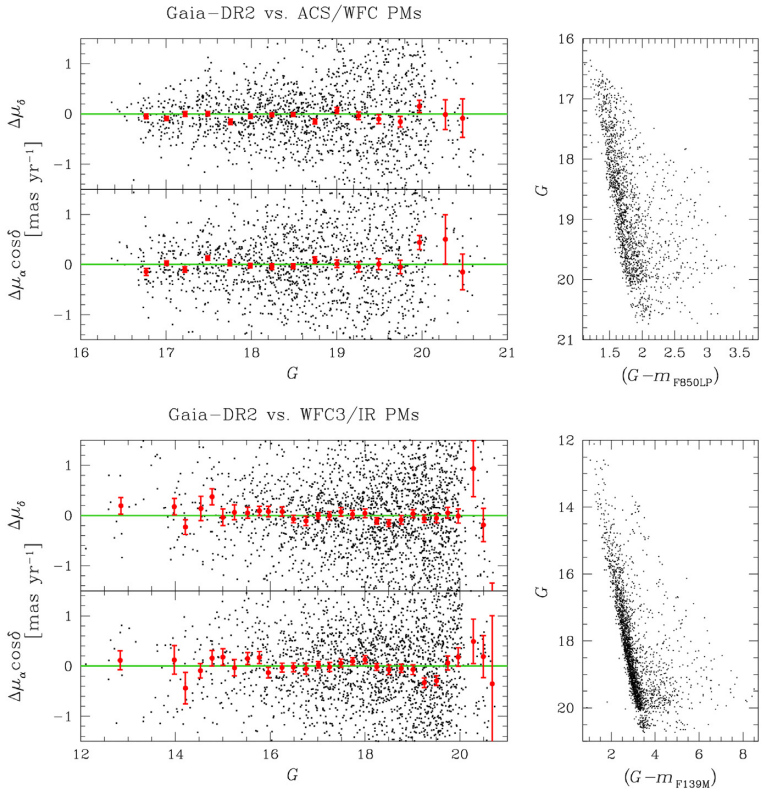

Figure A5. The figure shows that most of the colour-related PM trends visible in Fig. A4 are mainly due the *Gaia*-DR2 PMs of faint stars. In the left-hand panels, we show the PM difference between the *HST* (top panels for the ACS/WFC and bottom panels for the WFC3/IR) and *Gaia* data as a function of the G magnitude. Largest scatters are visible at $G > 18.5$. These stars are the reddest objects in the CMDs on the right. This finding supports the idea that the colour trends in Fig. A4 are mainly caused by *Gaia*-DR2 PMs.

APPENDIX B: COMPARISON BETWEEN WFC3- AND ACS-BASED PMS

The comparison between the PMs obtained with the ACS/WFC and WFC3/IR data for all stars in common between the two data sets (bottom panels of Fig. B1) shows that there is a systematic trend. Most of the stars responsible of the deviation from the 1:1 relation have a bright neighbour in the WFC3/IR data. These stars can easily be removed from the sample by using two diagnostic parameters described in Section 2: the RADXS parameter ($|\texttt{RADXS}| < 0.04$) and the fraction of neighbour flux within the fitting radius before neighbour subtraction ($o < 1$). After removal, the comparison between the two sets of PMs is improved (top panels).

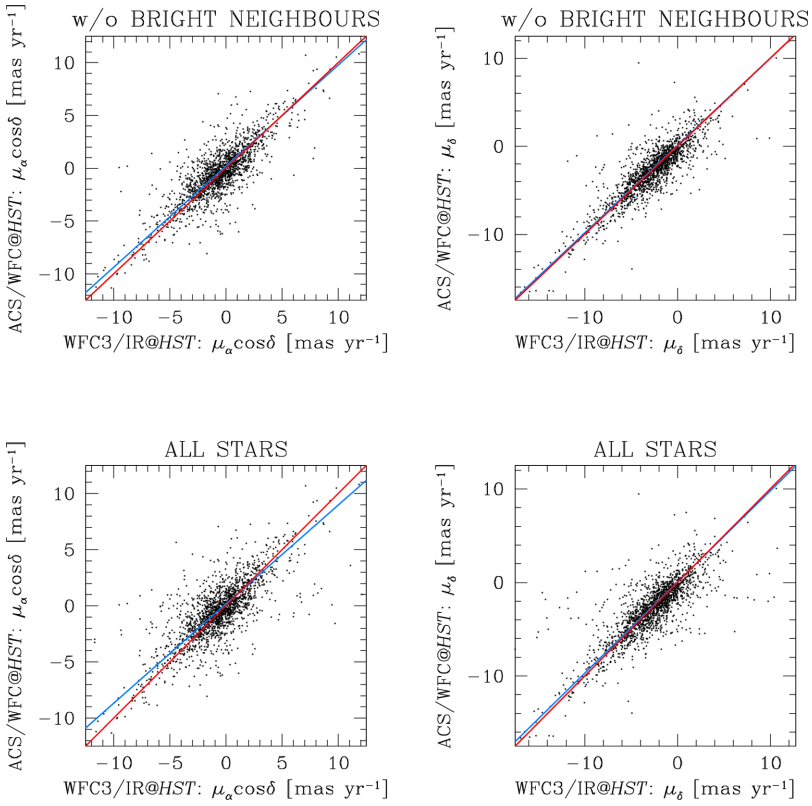

Figure B1. Similar to Fig. A1, but for the WFC3/IR- and ACS/WFC-based PMs. The comparison obtained by using only stars without bright neighbours is presented in the top panels. The bottom panels show all stars in common.

APPENDIX C: DESCRIPTION OF THE ASTRO-PHOTOMETRIC CATALOGUES

We release a photometric catalogue for each instrument/epoch, and a PM catalogue for each instrument. The ID entries in the astrometric catalogues are the internal IDs of the reduction process.

Table C1 shows the first 10 lines of the GO-12915 WFC3/IR data (all other photometric catalogues contain the same column information). VEGA magnitudes can be converted into instrumental magnitudes (at a 1-s exposure time) by subtracting the zero-points listed in Table C2.

The first 10 lines of the WFC3/IR PM catalogue are shown in Table C3. The X and Y positions (pixel scale 50 mas pixel^{-1}) are the average between the first- and second-epoch positions obtained in the PM-computation process. PM errors equal to 99.99 mas yr^{-1} refer to PMs obtained with only measurement in at least one epoch.

Table C1. First 10 lines of the WFC3/IR F139M photometric catalogue based on the GO-12915 data.

VEGA mag (1)	rms mag (2)	QFIT (3)	o (4)	RADXS (5)	n_f (6)	n_u (7)	Local sky (8)	Local-sky rms (9)
16.6034	22.6732	0.999	0.0030	−0.0132	1	1	2.15	0.72
13.9209	1.9165	0.999	0.0003	0.0052	1	1	0.00	0.00
16.8250	27.8072	0.999	0.0005	0.0177	1	1	2.02	0.28
15.9924	12.9156	0.998	0.0004	0.0175	1	1	3.23	0.99
13.7264	1.6022	0.999	0.0000	0.0126	1	1	9.34	3.65
17.1066	0.0019	0.998	0.0056	−0.0101	2	2	2.14	0.92
16.6040	22.6854	1.000	0.0023	0.0056	1	1	2.04	0.57
16.6611	0.0210	0.999	0.0014	−0.0070	2	2	1.97	0.40
12.9643	0.7941	0.999	0.0000	−0.0189	1	1	18.41	8.27
16.3636	18.1810	0.999	0.0019	0.0146	1	1	2.30	0.50
[...]	[...]	[...]	[...]	[...]	[...]	[...]	[...]	[...]

Notes. Columns: (1) VEGA magnitude; (2) magnitude rms; (3) QFIT; (4) fraction of neighbour flux within the fitting radius before neighbour subtraction; (5) excess/deficiency of flux just outside of the fitting radius with respect to that expected from the PSF; (6) the number of single exposures a star was found; (7) the number of measurements used to compute the photometric quantities of a star; (8) local sky (in counts); (9) local-sky rms (in counts).
(i) Stars are ordered as in the corresponding PM catalogue. (ii) Stars measured in only one image have a magnitude rms equal to 9.99 mag. (iii) Stars with rms mag, QFIT, o, RADXS, n_f, and n_u equal to 0 are saturated in the majority of the images in which they were found.

Table C2. Adopted zero-points used to calibrate our instrumental photometry into the VEGA-mag flight system.

GO	Instrument/camera	Filter	Zero-point
12915	WFC3/IR	F139M	23.3039
12915	ACS/WFC	F850LP	24.2151
13771	WFC3/IR	F139M	23.3089
13771	ACS/WFC	F850LP	24.2161

The average temporal baseline is defined as the difference between the average time of the first- and second-epoch images used to measure PMs. The values n_1 and n_2 are the numbers of images used to compute the averaged first- and second-epoch positions, respectively.

Table C3. First 10 lines of the WFC3/IR PM catalogue.

R.A. (deg) (1)	Dec. (deg) (2)	X (pixel) (3)	Y (pixel) (4)	$\mu_\alpha \cos\delta$ (mas yr^{-1}) (5)	$\sigma_{\mu_\alpha \cos\delta}$ (mas yr^{-1}) (6)	μ_δ (mas yr^{-1}) (7)	σ_{μ_δ} (mas yr^{-1}) (8)	Δtime (yr) (9)	n_1 (10)	n_2 (11)	ID (12)
266.290 5382	−29.250 1896	19 418.5218	1236.5295	−1.872 99	99.990 00	−3.614 88	99.990 00	2.8222	1	1	3
266.289 5192	−29.250 1574	19 482.5327	1238.8051	−2.563 58	99.990 00	−4.898 45	99.990 00	2.8222	1	1	4
266.293 5075	−29.250 1091	19 231.9894	1242.4437	−1.854 39	99.990 00	−4.210 34	99.990 00	2.8222	1	1	5
266.293 9944	−29.249 9806	19 201.4104	1251.7144	−7.620 24	99.990 00	−2.581 83	99.990 00	2.8222	1	1	6
266.293 8486	−29.249 5592	19 210.5888	1282.0495	−2.513 80	99.990 00	−9.971 58	99.990 00	2.8222	1	1	7
266.291 1804	−29.249 3321	19 378.2178	1298.2947	−2.777 95	1.398 70	−3.347 88	1.057 66	2.8222	2	2	9
266.295 5196	−29.248 9240	19 105.6429	1327.8556	−2.347 27	99.990 00	−2.633 57	99.990 00	2.8222	1	1	10
266.290 2060	−29.248 8892	19 439.4495	1330.1431	−2.939 34	1.534 31	−2.571 90	0.885 52	2.8222	2	2	11
266.287 0774	−29.248 8844	19 635.9957	1330.3597	−8.509 08	99.990 00	−3.359 06	99.990 00	2.8222	1	1	12
266.295 1208	−29.248 8618	19 130.6988	1332.3214	−5.236 83	99.990 00	−6.110 44	99.990 00	2.8222	1	1	13
[...]	[...]	[...]	[...]	[...]	[...]	[...]	[...]	[...]	[...]	[...]	[...]

Notes. Columns: (1) Right ascension; (2) Declination; (3) X position; (4) Y position; (5) PM along $\alpha\cos\delta$; (6) PM error along $\alpha\cos\delta$; (7) PM along δ; (8) PM error along δ; (9) Average temporal baseline; (10) the number of measurements in epoch 1; (11) the number of measurements in epoch 2; (12) ID.
(i) Stars measured in only one image have a PM error of 99.99 mas yr^{-1} in each coordinate.

APPENDIX D: LIST OF CONFIRMED, CANDIDATE, AND NON-MSS

Table D1 presents the list of confirmed MSs, candidate MSs, and non-massive objects analysed in Section 5.

Table D1. First 10 lines of the list of confirmed MSs, candidate MSs, and non-massive objects analysed in Section 5.

R.A. (deg) (1)	Dec. (deg) (2)	ID (3)	List (4)	Alternative ID (5)
266.290 7358	−29.236 9064	189	Primary	151
266.287 3217	−29.204 9508	1616	Primary	147
266.279 3346	−29.200 1464	1869	Primary	53
266.341 1210	−29.199 8483	1886	Primary	49
266.270 1831	−29.196 2723	2061	Other	2MASS J17450483-2911464
266.261 9529	−29.149 9028	5289	Primary	50
266.319 6554	−28.973 6557	13 644	Primary	134
266.370 3120	−28.957 3639	14 221	Other	XID #947
266.381 1732	−28.954 6972	14 332	Primary	36
266.400 5566	−28.944 0693	14 733	Primary	111
[...]	[...]	[...]	[...]	[...]

Notes. Columns: (1) Right ascension; (2) Declination; (3) ID; (4) original list (see Section 5); (5) ID in the original list in column (4).
(i) 'Primary' and 'Secondary' are the lists of confirmed and potential, respectively, Paschen α emitters of Dong et al. (2011). 'Other' is the collection of objects from other sources (see Section 5). (ii) Objects with alternative IDs in the 'Other' list starting with 'C' are from Clark et al. (2018). (iii) We refer to the papers listed in Section 5 for the spectral-type characterization of these stars.

This paper has been typeset from a TEX/LATEX file prepared by the author.